HHS Public Access

Author manuscript

Cancer Cell. Author manuscript; available in PMC 2022 November 08.

Published in final edited form as:

Cancer Cell. 2021 November 08; 39(11): 1464–1478.e8. doi:10.1016/j.ccell.2021.09.005.

Human prostate cancer bone metastases have an actionable immunosuppressive microenvironment

Youmna Kfoury[1,2,3,*], **Ninib Baryawno**[1,2,3,4,*,§], **Nicolas Severe**[1,2,3,*], **Shenglin Mei**[5,*], **Karin Gustafsson**[1,2,3,*], **Taghreed Hirz**[1,2,3,*], **Thomas Brouse**[1], **Elizabeth W. Scadden**[1], **Anna A. Igolkina**[6], **Konstantinos Kokkaliaris**[1,2,3], **Bryan D. Choi**[7], **Nikolas Barkas**[5], **Mark A Randolph**[8], **John H. Shin**[7,†], **Philip J. Saylor**[9,†], **David T. Scadden**[1,2,3,†], **David B. Sykes**[1,2,3,†], **Peter V. Kharchenko**[2,5,†,§,#], **Boston Bone Metastases Consortium**

[1]Center for Regenerative Medicine, Massachusetts General Hospital, Boston, MA, USA

[2]Harvard Stem Cell Institute, Cambridge, MA, USA

[3]Department of Stem Cell and Regenerative Biology, Harvard University, Cambridge, MA, USA

[4]Childhood Cancer Research unit, Dep. Of Children's and Women's Health, Karolinska Institutet, Stockholm, Sweden

[5]Department of Biomedical Informatics, Harvard Medical School, Boston, MA, USA

[6]St. Petersburg Polytechnical University, St. Petersburg, Russia

[7]Department of Neurosurgery, Harvard Medical School, Boston, MA, USA

[8]Division of plastic and reconstructive surgery, Massachusetts General Hospital, Boston, MA, USA

[9]Massachusetts General Hospital Cancer Center, Harvard Medical School, Boston, USA

Summary

[§]Correspondence: n.baryawno@ki.se and peter_kharchenko@hms.harvard.edu. [#]Lead contact: peter_kharchenko@hms.harvard.edu.

Author contributions

N.B., Y.K., N.S., D.B.S. and P.J.S. conceived the study. P.J.S. coordinated the multi-disciplinary teams and the IRB-approved protocol. N.B., N.S., Y.K., P.S., J.H.S., D.B.S., D.T.S. and P.V.K. directed the study. N.B., Y.K., N.S., K.G. and T.H. designed experiments. Sample collection methodology and surgeries were performed by J.H.S. Human malignant samples were collected, isolated and libraries prepared by N.B., Y.K., T.H., M.A.R. Y.K. collected human benign samples.. Flow cytometry was performed by Y.K., T.H. and K.G. N.B. N.S. established the bone metastatic mouse model. Y.K., N.S., K.G., K.K. and T.H. performed in vivo experiments. S.M., NIC.B. and P.V.K. performed the computational analysis. N.B., Y.K., N.S., S.M., T.H., K.G., J.H.S., P.J.S., D.T.S., D.B.S. and P.V.K. interpreted the data and wrote the manuscript. All authors read, edited and approved the manuscript.

[*,†]Contributed equally

Declaration of interests

P.V.K. serves on the Scientific Advisory Board to Celsius Therapeutics Inc. and Biomage Inc. D.T.S is a director and shareholder for Agios Therapeutics and Editas Medicines; a founder, director, shareholder and scientific advisory board member for Magenta Therapeutics and LifeVault Bio, a shareholder and founder of Fate Therapeutics, and a director, founder, shareholder for Clear Creek Bio, a consultant for FOG Pharma and VCanBio and a recipient of sponsored research funding from Novartis. D.B.S. is a founder, consultant and shareholder for Clear Creek Bio.

Bone metastases are devastating complications of cancer. They are particularly common in prostate cancer (PCa), represent incurable disease and are refractory to immunotherapy. We seek to define distinct features of the bone marrow (BM) microenvironment by analyzing single cells from bone metastatic prostate tumors, involved BM, uninvolved BM as well as BM from cancer-free, orthopedic patients and healthy individuals. Metastatic PCa is associated with multifaceted immune distortion, specifically exhaustion of distinct T cell subsets, appearance of macrophages with states specific to PCa bone metastases. The chemokine CCL20 is notably overexpressed by myeloid cells, as is its cognate CCR6 receptor on T cells. Disruption of the CCL20-CCR6 axis in mice with syngeneic PCa bone metastases restores T cell reactivity and significantly prolongs animal survival. Comparative high-resolution analysis of PCa bone metastases shows a targeted approach for relieving local immunosuppression for therapeutic effect.

Graphical Abstract

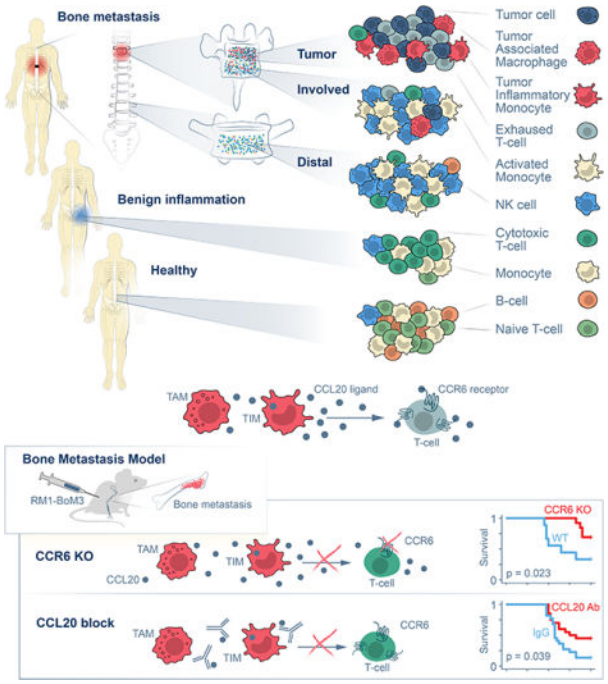

eTOC

Kfoury et al., identify an immune-suppressive microenvironment in human bone metastatic prostate cancer enriched in exhausted T cells and orchestrated by myeloid cells overexpressing CCL20. Pharmacological or genetic targeting of the CCL20/CCR6 axes in an animal model relieves the immune-suppressive state and extends the survival of metastatic tumor bearing mice.

Introduction

Prostate cancer frequently metastasizes to bone where, in the castration-resistant setting, 70 to 90% of patients have radiographically-detectable skeletal involvement (de Bono et al., 2011; de Bono et al., 2010; Halabi et al., 2016; Petrylak et al., 2004; Tannock et al., 2004). To date, bone metastases represent an incurable form of PCa and contribute

significantly to disease-specific morbidity and mortality (Xiang and Gilkes, 2019). In particular, metastatic involvement of the vertebral bodies can result in pathologic fracture and spinal cord compression leading to significant neurologic and functional disability, often necessitating surgical decompression and stabilization. Surgical decompression/stabilization and targeted radiation are used selectively. Approved bone-targeted systemic therapies offer some benefit: zoledronic acid and denosumab delay skeletal morbidity but do not improve overall survival (Saad et al., 2004). The radiopharmaceutical radium-223 offers a modest improvement in overall survival (Parker et al., 2013).

Spinal BM has long been known to be a primarily hematopoietic organ and represents a unique reservoir for several types of immune cells such as dendritic cells or myeloid derived suppressor cells (MDSCs), that have the ability to dramatically influence the trajectory of malignant disease. The critical role of the innate myeloid immunity in the tumor microenvironment goes well beyond its classical role of phagocytosis and antigen presentation. In addition to shaping the tumor adaptive immune response, myeloid cells impact response to cancer therapy (De Palma and Lewis, 2013; Engblom et al., 2016; Mantovani et al., 2017), promote angiogenesis (De Palma and Lewis, 2013; Lewis et al., 2016) and directly contribute to tumor progression and metastases through the secretion of growth factors and extracellular matrix degradation (Coffelt et al., 2016; De Palma and Lewis, 2013). Despite this, our incomplete understanding of myeloid cellular heterogeneity and plasticity, hinder the efficient translation of these findings towards improved disease outcomes.

The immune checkpoint therapies targeting CTLA4 and PD-1/PD-L1 that have proven to be effective against a wide range of tumors, have been unsuccessful in clinical trials in unselected PCa populations (Laccetti and Subudhi, 2017) despite the presence of T lymphocytes in the tissue (Chen et al., 2021). In particular, emerging evidence indicates that patients with PCa bone metastases (and other metastatic sites) are at a disadvantage when it comes to response to immune checkpoint therapies (Beer et al., 2017). This may in part be explained by the unique composition of the BM T cell population. Immunosuppressive T regulatory cells (Tregs) are particularly abundant in the BM space (Zou et al., 2004) and display a more activated phenotype (Glatman Zaretsky et al., 2017). In addition, when naïve T helper cells (T_H) become activated in the BM, the local cytokine environment appears to favor the development of T_H17 over T_H1 responses – a process that has detrimental impact on the success of immune checkpoint therapy (Jiao et al., 2019). Recent data suggest that the presence of bone metastases impairs immunotherapy efficacy in other cancers such as advanced non-small-cell lung cancer (Landi et al., 2019). Preclinical exploration of this phenomenon in metastatic castration resistant PCa (mCRPC) suggested that osteoclast resorption of bone releases TGF-B that restrains Th1 lineage development (Jiao et al., 2019). Altogether, this indicates that there is a clear need for new and more effective approaches for patients with bone metastatic PCa based on a better understanding of the immune microenvironment that is permissive of its growth and is a critical player in response to therapy.

Though the BM microenvironment is clearly hospitable to PCa, there have been multiple longitudinal barriers to gaining a better understanding of the supportive relationships

between cell types. Bone biopsies present challenges centered on patient discomfort, feasibility, and sample quality after decalcification. Imaging biomarkers of bone metastatic response to systemic therapy are substantially limited. Preclinical models of PCa metastatic to bone have historically been limited as well. Finally, bulk sequencing of tumor tissue has yielded important insights but is limited by its inability to characterize subpopulations and specific expression of ligands and receptors of tumor, immune, and stromal cells. In current clinical practice, the tumor tissue that is removed surgically in cases of spinal cord compression has little diagnostic utility. In this study, we systematically collect this fresh tissue for cell isolation, phenotyping, and expression analysis with single-cell RNA sequencing (scRNA-seq) to assess populations of immune, tumor, and stromal cells in this environment. We hypothesize that an improved understanding of immune cell support of malignant cells within the BM will identify areas of vulnerability amenable to therapeutic intervention.

Results

Widespread alteration of the BM by PCa metastases

Availability of fresh clinical PCa bone metastatic samples is essential to the study of relationships between cancer cells and the BM microenvironment. Bone sampling by needle biopsy can be technically challenging and provides scant quantities of tissue. We therefore developed an inter-disciplinary workflow to obtain tissue from emergent clinically-indicated surgeries for rare cases of spinal cord compression due to epidural extension of tumor or pathologic fracture of a vertebral body. We collected matched sets of tissue fractions from each patient: solid metastatic tissue (*Tumor*), liquid BM at the vertebral level of spinal cord compression (*Involved*), as well as liquid BM from a different vertebral body distant from the tumor site but within the surgical field (*Distal*) (Fig. 1A). This allowed for a comparison within the same individual, controlling for inter-individual variation and potential systemic effect for administered therapy. All patients had a historic diagnosis of PCa and had standard pathologic evaluation to confirm PCa in the BM within tissue sampled at the time of surgery (Fig. 1B, S1A, Table S1). Additionally, each had a preoperative magnetic resonance imaging (MRI) of the spine showing obvious evidence of tumor causing spinal cord compression (Fig. 1C, S1B). We focused on patients receiving ongoing therapy with an androgen receptor (AR)-targeted regimen, including GnRH agonists, antiandrogens, and androgen biosynthesis inhibition. Key clinical characteristics of the examined patients, including age, prostate-specific antigen levels, and treatment status are shown in Table S1. Bone marrow samples from patients undergoing hip replacement surgery (*Benign*) served as a non-malignant control group. The transcriptional composition of all samples was assessed using scRNA-seq for nine cancer patients and seven *Benign* BM controls. The measurements yielded on average of 2,490 cells per sample, detecting on average 3,952 molecules per cell (Table S1). Integration of all samples using *Conos* algorithm (Barkas et al., 2019) revealed a rich repertoire of immune cells and ongoing hematopoiesis with HSC/progenitor populations giving rise to B cell, monocyte, and erythroid lineages (Fig. 1D–F, Table S2). The T cell population was disconnected (Fig. 1E), which is expected as T cell maturation occurs outside of the BM. Granulocytes, whose abundance was quantified using flow cytometric analysis (Fig. S1D), were absent in the single-cell data, reflecting a

known cell lineage limitation of the utilized single-cell protocol (Chen et al., 2018). The stromal subpopulations, mostly captured within the *Tumor* fraction, included endothelium, pericytes, osteoblasts, osteoclasts as well as the tumor cells themselves (Fig. 1E,G,H).

The tumor cells, which were annotated based on expression of key PCa markers (KLK4, KLK2, AR) (Fig. 1F), displayed patient-specific chromosome-scale deviations of expression magnitudes indicative of the presence of CNVs (Patel et al., 2014; Tirosh et al., 2016) (Fig. S2A), and notable inter-individual variation of expression patterns (Fig. 2A, S2C). Even in *Tumor* fractions, the overall abundance of the tumor cells was relatively low (3.4% on average, Fig. S2B), owing to a rapid tissue dissociation protocol utilized. While harsher protocols can be used to increase the detection of tumor and stromal population (Henry et al., 2018), we utilized a rapid protocol to achieve comprehensive coverage of the immune compartment with minimal perturbations. Tumor cells were also detected in some of the *Distal* fractions, reflecting diffuse BM involvement in certain patients (Fig. S2B). Tumor cells exhibited strong patient-specific expression differences (Fig. 2A), however, analysis of intra-tumoral heterogeneity revealed four major aspects of tumor cell variation that were shared by different patients (Fig. 2B–D). Three of the aspects (IC2–4) reflected variation in the metabolic activity related to protein, nucleic acid, and ribosomal metabolism. The remaining aspect (IC1), however, was driven by transcription of genes associated with cell differentiation and AP-1 signaling, including IER2, JUNB, and SOX4, that have all been shown to facilitate motility and invasion of metastatic cells (Bilir et al., 2016; Hyakusoku et al., 2016; Neeb et al., 2012; Tiwari et al., 2013). This aspect was strongly enriched for functions related to vasculature development, epithelial cell differentiation, as well as regulation of hematopoietic regulation (Fig. S2D). This AP-1 related aspect of intratumoral variation clearly separated subpopulations within the metastatic tumors of multiple patients (Fig. S2E).

The presence of metastases significantly altered the immune cell composition of the BM. Relative to *Benign* controls, the three cancer fractions showed a striking depletion of B lymphopoiesis (Fig. 1G, 3A, S1E). The *Tumor* fraction had an increase in the proportion of macrophages compared to the *Involved/Distal* fractions (Fig. 1H). As expected, the solid *Tumor* fraction also showed more abundant endothelial, pericyte, osteoblast, and tumor cell populations (Fig. 1H, S3A). As analysis of simple cell proportions can be skewed by a single large-scale change, such as depletion of a large B cell compartment, we confirmed the shifts mentioned above using a more robust compositional data analysis technique (Fig. S3C).

Complementary to the shifts in the frequency of cell types (Fig. 3A, S3A), scRNA-seq data also captured the transcriptional state permitting an examination of expression differences. With the exception of the *Benign* controls, the overall similarity of cell states in different samples reflected patient-specific signatures (Fig. S3B). The extent of inter-patient differences was smallest for the *Benign* controls, and incrementally increased towards the site of metastases (*Distal* to *Involved* to *Tumor* fraction) (Fig. 3B). This significant increase in the inter-patient variability in cancer, and the *Tumor* fraction in particular, demonstrates the divergent impact of metastases on the BM across individuals. Nevertheless, we find that for many cell types the expression difference between cancer and control groups significantly exceeds the magnitude of inter-individual variation within the groups (Fig.

3C), underscoring the marked impact of the presence of the metastases on the transcriptional states of different populations. The HSC/progenitor population (*Progenitors*) was among the most affected. Analysis of differentially expressed genes between *Involved* BM with the *Benign* controls revealed pronounced downregulation of cell cycle in the *Progenitor* cells in the *Involved* samples, complemented by upregulation of translation and immune activation functions (Fig. 3D,E, S3D–G). Beyond the changes in the *Progenitor* population, we observed widespread upregulation of pathways related to stress response (ribosome assembly, protein localization to ER, particularly noticeable in dendritic, NK and NKT cell populations), as well as immune activation (most significant in T helper, naïve T and mature B cells) (Fig. 3D,E, S3F,G). Observing such broad impact of metastases across different cellular compartments, we focused our analysis on the detailed changes affect the two major immune compartments, myeloid and T cells. For this purpose, we excluded two patients (BMET-10 and BMET-11) that had received Radium 223 treatment (Table S1), as the detailed patterns of expression signatures and population composition appeared to be distinct (Fig. S1F, S2F,G). The general trends described above, however, remained consistent with or without the inclusion of these two patients.

Inflammatory monocytes and immunosuppressive macrophages in tumors

The myeloid cells have been implicated in supporting tumor progression in certain cancers (Coffelt et al., 2016; Lewis et al., 2016). Focused examination of the myeloid compartment revealed substantial population shifts between *Benign* and malignant fractions (Fig. 4A,B, S4A,B). While *Benign* controls mostly contained resting monocytes, the monocytes of both *Involved* and *Distal* fractions expressed genes indicative of an activated and proliferative state in cancer patients (Mono-2, myeloid cell activation, GO:0002275 $P<10^{-16}$). Striking changes were observed in the *Tumor* samples, with the appearance of prominent populations of Tumor Inflammatory Monocytes (TIMs), and Tumor Associated Macrophages (TAMs) (Fig. 4B, S4B, Table S3) exhibiting high expression of monocyte and macrophages signatures respectively (Fig 4C,D and Fig S4C). These findings were validated by flow cytometric analysis of independent samples (Fig. 4E, S1D, Fig. S4D).

The TAM population had an expression pattern characteristic of M2 macrophages (Azizi et al., 2018) (Fig. 4F,G) which have been shown to suppress anti-tumor immune responses across a broad range of tumors (DeNardo and Ruffell, 2019). Accordingly, TAMs express anti-inflammatory cytokines (TGFB1, IL-10, Interleukin 1 receptor antagonist IL1rn) (Sanjabi et al., 2009) as well as factors implicated in cancer growth and invasiveness (CCL2, CCL3, CCL4, VEGF, MMPs) (Bachelder et al., 2002; Merchant et al., 2017; Pellikainen et al., 2004) (Fig. 4F). In contrast to the TAM immunosuppressive signature, TIMs had a pro-inflammatory monocyte signature with high expression of pro-inflammatory cytokines such as IL1-B and TNF (Fig. 4F,H, S4G) (Becking et al., 2015; Smillie et al., 2019).

The TIM and TAM populations that we observed in the *Tumor* fractions closely paralleled *ex vivo* effects on peripheral blood monocytes of tumor-secreted factors (Vlaicu et al., 2013). The cells expressed epidermal growth factor-like ligands (epiregulin (EREG) in TIMs, HB-EGF in TAMs) and a common repertoire of interleukin-6-like JAK/STAT3 pathway activators (IL-6, Oncostatin-M (OSM)) (Fig. 4F). Both signaling modalities support

tumor growth directly as well as indirectly by suppressing the activation of CD8+ cytotoxic T lymphocytes (CTLs), expanding suppressive Treg cells, promoting M2 macrophage polarization and differentiating myeloid cells into MDSCs (Huynh et al., 2017). TIMs and TAMs also expressed inhibitors of the pro-inflammatory nuclear factor-*k*B pathway (NFKBIA, NFKBIZ, TNFAIP3) (Lawrence, 2009) (Fig. 4F). The presence of these TIM and TAM expression signatures are associated with significantly worse prognosis for patients across a broad range of cancer types (Fig. S4E).

To examine the extent to which the observed expression changes may be specific of prostate-origin metastases, we have carried out additional scRNA-seq analysis of lung carcinoma and melanoma bone metastasis. We also compared the myeloid populations observed in the prostate-origin metastases with published data on primary PCa (Chen et al., 2021), as well as other cancers (Lambrechts et al., 2018; Peng et al., 2019; Witkowski et al., 2020; Zhang et al., 2019), in order to examine potential prostate-specific and pan-cancer signatures. Joint alignment of these datasets identified presence of subpopulations analogous to TIM and TAM across most cancers (Fig. 5A). The details of their molecular state, however, differed from the populations observed in the PCa bone metastases depending on their origin and anatomical context. The TIM population in the PCa metastases shows significantly stronger inflammatory signature, compared to all other examined cancers (Fig. 5B). For TAM, the M2 polarization observed in the metastatic context was comparable to those seen in other tumors (Fig. 5C). For most cancers, the detailed molecular profiles of these analogous populations differ substantially (Fig. 5D,E). The bone metastases of other solid tumors, in particular melanoma, showed most similar TIM and TAM populations. Interestingly, acute lymphoblastic leukemia samples were very distinct, despite sharing BM localization. Beyond that, the most similar TIM and TAM profiles were seen in the primary PCa (Fig. 5D,E). Systematic differences, however, were seen even on the small panels of cytokine markers, such as expression of *TNF*, *IL1A* or *CCL3*/*CCL4* that was seen in the primary PCa, but absent in the metastatic context. Assessment of the overall transcriptional similarity shows a gradual spectrum of expression differences that likely reflect a combination of cancer-specific and context-specific features (Fig. 5F,G).

Expansion of dysfunctional cytotoxic T lymphocyte subpopulation in bone metastases

Detailed analysis of lymphocytes revealed the expected subsets, $CD4^+$ T helper (T_H) and Tregs, CTLs, as well as NK and NKT cells (Fig. 6A, Fig. S5A, Table S2,3). The smallest population of $CD8^+$ CTLs expressed high levels of *CCR7*, *LEF1* and *SELL*, indicating that these are antigen-inexperienced, naïve cells (Fergusson et al., 2016; Picker et al., 1993; Willinger et al., 2006) (Fig. S5A). The CTLs could be further subdivided into two subtypes: CTL-1 expressing effector T cell genes such as *KLRG1*, *GZMK* and other cytotoxicity mediators, whereas CTL-2 are characterized by an effector/memory-like transcriptional profile including *IL7R* and *KLRB1* (Fig. 6B) (Fergusson et al., 2016; Zhang et al., 2018). We also identified CCR7 expressing naïve CD4+ cells, whereas the mature T helper cell compartment appeared to be a mix of T_H1 and T_H17 cells ($T_H1/17$) expressing *CXCR3* and *CCR6* respectively (Fig. S5A) (Zhang et al., 2018). Unfortunately, the data did not provide sufficient resolution to further distinguish the two populations.

The proportions of the CTL, and T_H / $T_{H1/17}$ populations significantly increased in the *Tumor* fraction in comparison to the *Distal* and *Involved*, whereas other T cell types were found to be unchanged (*e.g.* Tregs) or decreased in the *Tumor* (*e.g.* naïve T cells) (Fig 6C,D, S5B). The abundance of activated effector T cells and Tregs was also high in the *Benign* controls (Fig 6C,D, S5B), likely reflecting the known inflammation in these osteoarthritis patients. To control for the sustained inflammation apparent in the Benign controls, an additional set of BM samples from *Healthy* individuals (Oetjen et al., 2018) were added to the analysis and revealed significantly lower abundance of these populations, offset by higher proportion of $CD4^+$ naïve cells (Fig. 6D). The functional state of these T cell subsets was also impacted, in particular CTL-2 in the *Tumor* fraction exhibited reduced cytotoxicity expression signature in combination with a pronounced T cell exhaustion profile, typical of dysfunctional CTL commonly observed in tumors (Lee et al., 1999; Li et al., 2019) (Fig. 6E, S5C–E). The level of T cell exhaustion observed in the CTL-2 cells of the *Tumor* fraction was significantly higher than that of the *Benign* controls, highlighting the distinction between sustained benign inflammation and the metastatic context. The NK cell population showed a complementary pattern, with high abundance in the *Involved* and *Distal* samples, but not in *Benign* and *Tumor* fractions (Fig. 6C,D) - an observation that was further validated by flow cytometric analysis (Fig. 6F, S1E). This suggests that although NK cells can be recruited to the general area of bone metastases, they may fail to infiltrate the tumor.

Coordination between myeloid and lymphoid compartments

The observed deficiencies of cytotoxicity in the proximity of the tumor may arise through repressive actions by other immune cells (Munn and Bronte, 2016). For instance, we find that the Tregs, which typically act to suppress immune response (Woo et al., 2002), showed increased activity signatures at the site of metastases (Fig. S5F). The complex patterns of immune signaling are also likely to involve the myeloid compartment. Indeed, considering variation of TAM and TIM abundance among patients (Fig. S4F) we find that an increased proportion of TAMs at the site of metastases is correlated with CTL-2 exhaustion (Fig. 6G). This association was further supported by analysis of exhaustion and TAM expression signatures in bulk RNA-seq data (Fig. 6G, S5H). While the observed associations suggest that TAM or TIM subsets may be directly affecting T cell state, identifying a specific signaling channel through which communication takes place is challenging due to lack of methodology. The space of potential interaction channels is extensive: screening a database of ligand and cognate receptors (Efremova et al., 2020) for those expressed in myeloid and T lymphoid compartments, respectively, we find 241 potential channels (39 for TAM, 29 for TIM, Fig. 6H, Table S4). To prioritize likely candidates, we applied additional filtering criteria, requiring up-regulation of the receptor expression in *Tumor* in comparison to *Benign* controls, and high levels of ligand expression in the corresponding myeloid population, reducing the number of potential channels to 7 (Fig. 6I). Of the cytokines that were expressed within the TIM and TAM cells of the *Tumor* fraction, CCL20 was one of the most highly expressed (Fig. 4F, 6J, S4G), and its cognate receptor CCR6 was predominantly expressed on Treg and $T_H1/17$ cells (Fig. 6K, S6A). Studies of other cancers have demonstrated that CCL20 signaling can promote tumor growth, invasiveness and chemoresistance (Lee et al., 2017; Lu et al., 2017; Walch-Ruckheim et al., 2015) by recruitment of Tregs and/or T_H17 cells (Walch-Ruckheim et al., 2015; Wang et al.,

2019). CCL20 protein levels were confirmed in different BM fractions with ELISA (Table S5). CCL20 has been shown to be expressed on primary PCa tumor cells and in stromal fibroblasts within the tumor microenvironment (Beider et al., 2009; Walch-Ruckheim et al., 2015). However, in the metastatic samples, CCL20 was expressed by the TIM and TAM populations, and was absent from the tumor cells (Fig. 6J). Overall, the direct role of the CCL20-CCR6 axis in human PCa bone metastases is unclear.

CCL20-CCR6 signaling leads to T lymphocyte exhaustion

To investigate the impact of CCL20-CCR6 signaling axis in PCa bone metastases, we developed a syngeneic mouse model based on the RM1-BM cell line derived from C57BL/6 RM1 PCa cells (Power et al., 2009; Thompson et al., 1989). These cells were sequentially injected into C57BL/6J wild-type (WT) mice to generate a highly penetrant bone tropic PCa cell line, RM1-BoM3, that induced osteolytic and osteoblastic lesions as shown by micro-computed tomography (microCT) and radiography (Fig. S6B–E). The RM1-BoM3 cell line does not express CCR6 and shows low levels of CCL20 expression (Fig. S6F–H). The changes of the BM accompanying these mouse tumors mirrored that observed in the human samples, with expansion of CD8+ T cells carrying *Pdcd1* and *Lag3* exhaustion signature in the lymphocyte compartment (Fig. 7D, S6I), and appearance of large macrophage populations, including those with M2 signature, in the myeloid compartment (Fig. S7A–C). Using this model, we demonstrate that the absence of CCR6 improved survival of bone metastases bearing mice when compared to controls (Fig. 7A,B). Likewise, administration of CCL20 blocking antibody to WT mice with PCa bone metastases resulted in a survival advantage in comparison with isotype treated controls (Fig. 7C). Single-cell analysis on T cells from the bone metastases isolated from WT and CCR6-KO mice showed average reduction in Active Tregs and Exhausted CTLs with a concomitant increase in Naive CTLs (Fig. 7D, S6I). Similarly, the myeloid compartment in the CCR6-KO mice showed decrease of the M2 macrophage population (Fig. S7A).

These results suggest that blockade of the CCR6-CCL20 axis counteracts immunosuppression in the bone metastatic tumor microenvironment. In order to further confirm this impact on the CTLs, flow cytometric analysis of T cell populations was performed on BM from bone metastases bearing WT and CCR6-KO mice as well as tumor naive WT mice. This revealed a significant increase in the frequencies of both CD4+ T_H cells and CD8+ CTLs in the BM of CCR6-KO mice with PCa bone metastases (Fig. S7D). The infiltrating CTLs also appeared less exhausted in the CCR6-KO mice as evidenced by reduced cell surface levels of exhaustion markers PD-1 and Lag3 (Fig. 7E, S7E,F). Notably, the CCR6-KO CTLs were found to display a similar exhaustion profile as their tumor naive counterparts, suggesting that CTL activity is unimpeded at the tumor site after inhibition of CCR6-CCL20 signaling. To test this, CTLs were sorted from WT and CCR6-KO mice with tumor as well as from tumor naive WT mice and stimulated *in vitro*. After 96 hours, WT CTLs produced less IFNg and proliferated at a significantly lower rate than both tumor naive and CCR6-KO cells (Fig. 7F,G, S7G), indicating that increased expression of exhaustion markers displayed by these cells, translates into a reduced functionality. In contrast, CTLs from CCR6-KO mice exhibited significantly higher level of IFN-g compared to Naive or

WT tumor bearing mice (Fig. 7F) indicating the re-activation of CTLs upon CCR6:CCL20 blocking.

Discussion

Together, the unique set of samples analyzed provides a high-resolution landscape of human bone metastatic PCa, and its effect on BM. We show that the metastatic BM is distinct from either the immune activated state in individuals with osteoarthritis or healthy BM controls. The cancer-affected state has a broad but now defined set of cellular and molecular changes in the hematopoietic cells of the BM. These include a decrease in the cell cycle of primitive hematopoietic cells, and a dramatic decrease in B cells and B cell progenitors – a pattern that has been found to correlate with poor response to immune checkpoint blockade in other cancers (Xiong et al., 2020). The similarity of the *Involved* and *Distal* fractions suggests that these differences likely reflect systemic BM changes accompanying cancer. Systemic response likely accounts for the elevated levels of NK cells in both *Involved* and *Distal* vertebrae relative to controls, while their relative dearth in the tumor fraction likely reflects poor ability to infiltrate the tumor (Melaiu et al., 2019). In contrast, at the sites of solid tumor involvement, increases in monocyte/macrophage and the CTL and $T_{H1/17}$ T cell subsets were evident. Additionally, TIM and TAM populations expressed distinctive activation signatures, including TGFB1, and candidate signaling molecules that might affect T cells and their exhaustion signature. Interestingly, TGFB1 has been recently shown to be a molecular mediator for T_H cell polarization toward T_H17 in response to immune checkpoint therapy in the bone metastatic microenvironment and blocking it in combination with checkpoint inhibitors improved survival in a mouse model of PCa (Jiao et al., 2019). Further, exposure to the anti-androgen drug enzaluatamide was recently associated with an increased tumor-intrinsic TGFβ signaling and EMT signature in mCRPC (He et al., 2021), suggesting that resistance to anti-androgen treatment may be induced by TGFB1.

Through computational heuristics, we identify potential ligand-receptor pairs that may allow for communication between tumor-specific myeloid populations and T cells. We show how one such signaling axis, CCL20/CCR6, participates sufficiently in immune suppression that impairing it relieves the exhaustion phenotype and changes animal survival. This is particularly important because it raises the general prospect that inhibiting activating signals upstream of T cells can resolve cancer immune suppression. Identification of the CCL20/CCR6 axis as relevant for tumor control provides other important information with translational potential. This axis is implicated in a number of inflammatory and immune activated states, including autoimmune disease (Ranasinghe and Eri, 2018). The potential for modulating the axis to reduce the activated states of immune cells has been extensively explored and led to early stage clinical trials (Getschman et al., 2017; Robert et al., 2017). Specifically, anti-CCL20 was advanced to clinical testing with a focus on inflammatory disease (Bouma et al., 2017; Laffan et al., 2020). However, the drug did not advance in that setting (Hippe et al., 2020). In the context of cancer, the analysis of the CCL20-CCR6 signaling has focused the potential autocrine effect on the tumor cells (Beider et al., 2009; Ikeda et al., 2016; Ito et al., 2014; Lee et al., 2017). Our mouse data shows that such potential autocrine effects are distinct from the impact of this axis on the microenvironment, as animal survival was improved by CCR6 KO. In addition, CCR6 protein expression could

not be detected in the tumor cells of our mouse mCRPC model *in vitro* and *in vivo*. The data presented here suggest that the CCL20-CCR6 axis has potential, not as a direct suppressor of cancer cell growth as proposed previously, but as a means of relieving immune exhaustion. This would be of importance in the setting of bone metastases and PCa bone metastases in particular as these have shown little responsiveness to checkpoint blockade (Goswami et al., 2016). One promising approach is to augment of the existing immune checkpoint therapies with additional immune modulations, for instance inhibition of the TGF-β pathway (Jiao et al., 2019). It is notable, in this regard, that the immune activation and improved survival demonstrated in our animal model were achieved by the disruption of the CCL20-CCR6 axis alone.

The tumor-specific myeloid populations are the likely sources of CCL20 in the patient samples, where it is expressed by both TIM and TAM populations. In TIMs, the expression of CCL20 is strongly correlated with the overall TIM abundance (Fig. 7H). The distinctive TIM expression signature we identified in PCa bone metastases compared with other cancer types does raise the possibility that the CCL20/CCR6 axis is particularly important in PCa bone metastases. However, studies of other cancer metastases, in the bone and other sites will be needed to deconvolve the contributions of tumor-intrinsic properties and the host tissue. Similarly, relieving immune suppression by blocking the CCL20/CCR6 axis in the context of bone metastatic PCa raises the question whether this could be achieved at other metastatic sites or in primary tumors. Our preliminary data using a subcutaneous model of syngeneic PCa suggest that this might be the case (Data not shown) however better orthotopic and organ specific models are required to confirm this. It will also be important to consider systemic factors like androgen deprivation. Androgen deprivation therapy is universally applied to PCa patients as part of their standard treatment, and will require examination of rare outlier cases to define its role versus PCa itself in changing CCL20/CCR6. We believe the data presented here will provide a foundation for further exploring this and other signaling axes and cellular relationships that alter the immune response or the BM resulting in a tumor-permissive environment. Defining new approaches to the devastating clinical problem of PCa bone metastases is critically needed.

While the presented analysis provides a good representation of PCa bone metastases in general, a number of potential limitations should be noted. First, our study has focused exclusively on vertebral body metastases. The axial skeleton (vertebral bodies, pelvis, and ribs) is the most common site of metastases, in contrast to the appendicular skeleton (arms & legs) (Kakhki et al., 2013), however, the extent to which metastatic microenvironments may vary between vertebral bodies and other sites will require further investigations. Similarly, while comparison with osteoarthritis patients has allowed our study to control for pronounced effects of sustained inflammation, some of observed differences may also reflect the difference between vertebral and hip context, as well as osteoarthritis-specific biology. Second, the small sample size, due to the challenging nature and sparsity of bone metastatic PCa clinical samples, resulted in a lack of statistical power that masked critical elements of heterogeneity among patients. Similarly, the small number of tumor cells detected due to our choice of the dissociation protocol hindered the identification of potential tumor derived molecules that might be remodeling the immune microenvironment. Although single-cell data on different cancer types and contexts was sparse, the analysis

shown in Fig. 5 indicates that some of the observed changes may generalize to primary PCa, and bone metastases of different cancer types. It is likely that broader collections of metastatic and primary tumor measurements will allow to delineate contributions of tumor-specific and tissue-specific effects. Larger panels should also allow to explain features underlying the high inter-individual variability observed in the metastatic patients (Fig. 3B). Some of that variation likely stems from the presence of genetic aberrations in the tumor. The impact of treatment is also likely substantial. Here we focused on the most common class of patients – those receiving ongoing therapy with an androgen receptor (AR)-targeted regimen. Two individuals within that group stood out as outliers (Fig. S1F) also had a distinct therapy regiment: BMET-10 that was undergoing Radium-223, and BMET-11 who received Radium-223 previously and was currently receiving immune checkpoint inhibitor (pembrolizumab) treatment. BMET-10 sample, in particular, showed striking ablation of mature lymphocyte populations (Fig. S2F) – a potentially important observation given ongoing trials combining immune checkpoint inhibitor therapy with Radium-233.

STAR METHODS

RESOURCE AVAILABILITY

Lead contact—Further information and requests for resources and reagents should be directed to and will be fulfilled by the Lead Contact, Peter Kharchenko (peter_kharchenko@hms.harvard.edu).

Material availability—Further information and requests for resources and reagents should be directed to and will be fulfilled by David Scadden (david_scadden@harvard.edu).

Data and code availability—Further information and requests for data and code analysis should be directed to and will be fulfilled by the lead contact Peter V. Kharchenko (.peter_kharchenko@hms.harvard.edu). The expression datasets generated in this study are available through Gene Expression Omnibus with the accession number GSE143791. Interactive views of the single cell datasets, differential expression results, code notebooks, cell annotation and RData objects are available on the author's website at http://pklab.org/bonemet/.

EXPERIMENTAL MODELS AND SUBJECT DETAILS

Patient material—All human-subjects tissue collection was carried out with institutional review board (IRB) approval (Dana Farber/Harvard Cancer Center protocol 13–416 and Partners protocol 2017P000635/PHS).

Surgical approach and collection of tumor and BM specimens—In each case, the patient was brought to the operating room for clinically indicated decompression and stabilization in the setting of spinal cord compression related to metastatic PCa. Each patient consented to use of their tissue for research purposes. Bone marrow (*e.g. Involved*) and tumor samples were taken with the patient in the prone position under general anesthesia as the spine was approached posteriorly. After the levels of the spine were exposed and identified, a Jamshidi needle was malleted directly into the desired vertebral body and a

syringe connected to the needle was used to aspirate BM immediately upon cannulation. Cannulation of the vertebral body is standard prior to placing stabilizing instrumentation into the bone. By placing the Jamshidi needle directly into the bone, this ensures that the aspirate from deep within the vertebral body is not diluted by surrounding blood in the surgical field or surgical irrigation. The marrow aspirate taken from the vertebral body is then directly stored into collection tubes and transferred to the laboratory for further sample preparation. Similar technique was utilized for the distant vertebral body level samples (*e.g. Distal*). During each surgery, several vertebral body levels above and below the primary site of spinal cord compression are instrumented for stabilization. As such, there is access to numerous vertebral body levels through a single surgical approach. After the vertebral body marrow had been collected and the spine instrumented, the spinal cord is decompressed through a laminectomy. Epidural tumor that is circumferentially surrounding and compressing the spinal cord is taken directly from the field and transferred to the laboratory for further processing. Specimens were also submitted to pathology for standard confirmation of diagnosis of metastatic PCa.

Mice—CCR6-KO mouse models were developed by Deltagen, Inc and ordered from The Jackson Laboratory and (B6.129P2-*Ccr6*^{tm1Dgen}/J, #005793) and compared to age and gender match control mice C57BL6/J mice (#000664). All mice were maintained in pathogen-free conditions and all procedures were approved by the institutional Animal Care and Use Committee of Massachusetts General Hospital.

Mice with signs of bone metastases, as shown by bioluminescence imaging, were included in the survival study during which the health condition of the mice was scored. We adapted this scoring method from Nunamaker et al., to refine the endpoint for mice bearing bone metastases to minimize the pain and distress associated with bone metastases progression (Nunamaker et al., 2013). For each category, mice are scored from 0 to 3: Body posture, eye appearance and activity level. Mice with a score at 3 in one of the categories or a cumulative score >6 are euthanized. The health was assessed by the animal facility veterinarian and the lead investigator for the specific experiment. The main cause of euthanasia were eye lesions due to metastatic burden in the mandible. In addition, some of the mice developed leg paralysis. Otherwise, a general poor body condition was observed in moribund mice. Only mice showing signs of metastatic tumors in the bones by bioluminescence imaging were included in the survival studies. For inclusion of mice for survival studies, we image mice with bioluminescence imaging at week 1, 2 and 3, to ensure that the mice that are included in the study were continuing showing exponential growth.

Development of syngeneic PCa metastatic cell line—The bone metastatic RM1-BoM1 cell line, with a ~95% bone metastases penetrance, was obtained from the Power laboratory (Power et al., 2009) and was established from the parental PCa mouse model RM1 (RAS and c-Myc oncogenes were overexpressed in normal epithelial prostate cell and injected in syngeneic mice to form tumors) (Power et al., 2009). We enriched RM1-BoM1 cells negative for GFP and transduced with Tdtomato (LeGO-T2, Addgene #27342) and luciferase (pENTR-LUC, Addgene, #17473). We injected 2.10^5 RM1-BoM1 cells into the left ventricle of C57Bl/6 mice and monitored bone metastases development by sequential

bioluminescence imaging (bone metastases penetrance ~95%, mostly located in long bones, jaw and sometimes in the spine). Bone metastatic cells were harvested and selected for the Luciferase and Tdtomato expression. We used the mouse as a bioreactor and repeated a second round of injection and isolation of bone metastases cells in order to establish the RM1-BoM3 bone metastatic cells. The RM1-BoM3 sells were maintained in DMEM (Corning, 15–013-CV) complemented with 10% FBS (GIBCO by Life Technologies, A31605–01) and 1% Penicillin-Streptomycin (GIBCO by Life Technologies, 15140–122).

METHODS DETAILS

In-vivo Bioluminescence imaging—Mice were anesthetized by isoflurane inhalation with 2% O_2 and 4.5mg/mouse of D-luciferin K salt (RR labs Inc., San Diego) was administered by intraperitoneal injection. After 5 minutes, mice are imaged using a SPECTRAL Ami X allowing to detect the localization of the cancer cells in the mice and to measure the luciferase activity.

CCL20 blocking antibody treatment—C57BL6/J male mice (#000664) received an intraperitoneal injection of 45μg anti-CCL20 blocking antibody (R&D Systems clone 114908) or rat IgG isotype control antibody (R&D Systems, clone 43414) 1 day prior to intracardiac injection of RM1-BoM3 PCa bone metastases cells. The administration of blocking antibody and isotype control then continued on a twice-weekly basis until the end of the experiment.

In vitro stimulation of CD8+ CTLs—Sorted CD8+ CTLs were plated in 96-well plates in RPMI 1640 (Corning) supplemented with 10% FBS (Gibco), 10mM HEPEs (Gibco), 1% Penicillin/streptomycin (Gibco), 1% Non-essential amino acids (Gibco) and 50μM ß-mercaptoethanol. For cytokine production the plates were precoated with 2.5μg/ml CD3 antibody and 3μg/ml CD28 antibody whereas the CFSE labeled T cells were stimulated with Dynabeads mouse T activator CD3/CD28 (thermofisher scientific) at ratio 1:1. The cells were stimulated for 96 hour and cytokine production was thereafter assessed by intracellular flow cytometric analysis of IFNg.

Dissociation of tissues into single cells—All samples were collected in Media 199 supplemented with 2% (v/v) FBS. Single cell suspensions of the tumors were obtained by cutting the tumor in to small pieces ($1mm^3$) followed by enzymatic dissociation for 45 minutes at 37°C with shaking at 120 rpm using Collagenase I, Collagenase II, Collagenase III, Collagenase IV (all at a concentration of 1 mg/ml) and Dispase (2mg/ml) in the presence of RNase inhibitors (RNasin (Promega) and RNase OUT (Invitrogen). Erythrocytes were subsequently removed by ACK Lysing buffer (Quality Biological) and cells resuspended in Media 199 supplemented with 2% (v/v) FBS for further analysis.

ELISA measurement—CCL20 protein levels measured in plasma collected from BM of bone-metastatic PCa patients (*Involved*, *Distal*) and from BM of patients undergoing hip replacement surgeries (benign BM) using a commercially available enzyme-linked immunosorbent assay (ELISA kit R&D Systems, Minneapolis, USA) according to the

manufacturer's protocol. Absorbance was measured with Synergy HTX multi-mode reader (Bio-Tek).

Bone marrow processing—Bone marrow samples were filtered using 70 micron filter then centrifuged at 600 g for 7 minutes at 4°C. Plasma were collected followed by erythrocytes removal using ACK Lysing buffer (Quality Biological). Cells were resuspended in Media 199 supplemented with 2% (v/v) FBS for further analysis.

FACS sorting of human samples for single-cell RNA-sequencing—Single cells from tumor and BM samples subjected to RBC lysis were surface stained with anti-CD235-PE (Biolegend) for 30 min at 4°C. Cells were washed twice with 2% FBS-PBS (v/v) followed by DAPI staining (1 ug/ml). Flow sorting for live and non-erythroid cells (DAPI-neg/CD235-neg) was performed on a BD FACS Aria III equipped with a 100um nozzle (BD Biosciences, San Jose, CA) instrument. All flow cytometry data were analyzed using FlowJo software (Treestar, San Carlos, CA).

FACS sorting of murine samples—In order to obtain BM T cells and myeloid cells for single-cell RNA-sequencing from tumor bearing mice, RBCs were lysed and samples were subsequently incubated with anti-mouse Fc block (BD Pharmingen, 553142) for 10 minutes at 4°C. This was followed by surface staining for CD11b (myeloid cells) and CD3e (T lymphocytes) for 30 minutes at 4°C. The samples were then washed with 2% FBS-PBS (v/v) followed by resuspension in 2% FBS-PBS with 0.1μg 7-AAD. Flow sorting for live myeloid and T cells (7AAD- CD11b+ or CD3e+) was performed on a BD FACS Aria III equipped with a 70μm nozzle.

For evaluation of CTL proliferation response in mice with bone metastases, BM was stained with 3μM CellTrace CFSE (Thermo Fisher Scientific) in accordance with the manufacturer's instructions. This was followed by a 10 min incubation with anti-mouse Fc block and a 30 minute cell surface staining with anti-mouse CD4-APC/Cy7 and CD8-PE/Cy7 (Both from Biolegend). CFSE labeled CD8+ CTLs were subsequently sorted on a BD FACS Aria III (BD Biosciences, San Jose, CA) equipped with a 70μm nozzle. The rate of CFSE dilution was thereafter analyzed following 96 hours of *in vitro* stimulation. Proliferation rate was inferred by calculating the ratio of CFSE mean fluorescent intensity (MFI) at hour 0 and hour 96 for each individual sample.

For bulk RNA-sequencing RM1-Parental PCa cells were isolated from subcutaneous tumors whereas RM1-BoM1 and RM1-BoM3 cells were obtained from the BM of bone metastases bearing mice. Hematopoietic cells were excluded by staining for CD45-APC/Cy7 (Biolegend, clone 30-F11) and Ter119-APC/Cy7 (Biolegend) and DAPI enabled selection of live cells, lastly tumor cells were identified by GFP (RM1-Parental and RM1-BoM1) or tdTomato (RM1-BoM3). 500–1000 tumor cells were sorted into a 96-well plate containing lysis buffer for subsequent preparation of bulk RNA-sequencing libraries using the Smartseq2 protocol (Picelli et al., 2014).

FACS analysis—Independent samples from patients with PCa bone metastases were used for FACS analysis. Cells from human BM and tumor samples were surface stained with

lymphoid, myeloid and hematopoietic stem and progenitor antibody panels after blocking with anti human fc block (BD Pharmingen 564219) for 10 minutes at room temperature (Table S6) for 30 min at 4°C. Cells were washed twice with 2% FBS-PBS (v/v). Samples that were to eventually be fixed and permeabilized were stained with LIVE/DEAD fixable viability dye (Thermo Fisher Scientific, Waltham, MA). For the intracellular staining, to determine Treg infiltration, cells stained with lymphoid surface markers were fixed and permeabilized with Cytofix/Cytoperm (BD Biosciences, San Jose, CA) for 20 min at 4°C. Cells were then washed twice with 1× Perm/Wash buffer (BD Biosciences, San Jose, CA) and incubated overnight at 4°C with anti-FoxP3-PE. On the following day, cells were washed twice in Perm/Wash buffer and resuspended in 2% FBS-PBS (v/v) for analysis.

For analysis of CTL exhaustion in bone metastases bearing mice, BM cells were blocked with anti-mouse Fc block (BD Pharmingen, 553142) followed by surface staining with the murine T cell exhaustion panel (Table S7) for 30 min at 4°C. Cells were washed with 2% FBS-PBS (v/v) followed by resuspension in 2% FBS-PBS with 0.1μg 7-AAD.

CD8+ CTLs were assessed for their ability to produce IFNg after 96 hours of stimulation. Protein secretion was first inhibited 4 hours prior to cell isolation by the addition of GolgiStop (BD Biosciences, San Jose, CA) in accordance with the manufacturer's instructions. At the time of isolation the cells were blocked with anti-mouse Fc block (BD Pharmingen) followed by surface staining with murine T cell cytokine production panel (Table S6) for 30 minutes at 4°C. The cells were stained with LIVE/DEAD Fixable Blue dead cell stain (Thermo Fischer Scientific) for removal of dead cells. The samples were then fixed and permeabilized using BD Bioscience Fixation/Permeabilization Solution Kit (BD Biosciences) in accordance with the instructions supplied by the manufacturer. Lastly, the cells were stained with IFNg-AF700 for 60 minutes at room temperature.

Analysis of CCR6 expression on RM1-BoM3 cells was performed on both *in vitro* grown cells as well as on tumor cells isolated from the BM of tumor bearing cells. *In vitro* grown cells were first blocked with Fc block (BD Pharmingen) for 10 minutes at 4°C, followed by 30 minutes incubation with anti-mouse CCR6-BV421 (Biolegend, clone: 29–2L17). RM1-BoM3 cells from tumor bearing mice were Fc blocked (BD Pharmingen) for 10 minutes at 4°C and instead stained with anti-mouse CD45-APC/Cy7 (Biolegend, clone: 30-F11), and Ter119-PE/Cy7 (Biolegend) as well as CCR6-BV421 (Biolegend, clone: 29–2L17) for 30 minutes. The cells were washed and subsequently resuspended in 2% FBS-PBS with 300nM DAPI for analysis.

Flow cytometry was performed on a BD FACS Aria III (BD Biosciences, San Jose, CA) instrument. All flow cytometry data were analyzed using FlowJo software (Treestar, San Carlos, CA) and Prism software. Statistical analyses were performed as indicated and P values of ≤0.05 considered significant.

Healthy BM data—To provide an additional comparison to the samples from cancer patients and patients with benign inflammation that were collected as part of this study, we have also analyzed single-cell RNA-seq data for healthy individuals published by Oetjen *et al.* (Oetjen et al., 2018) The data was downloaded from GEO (GSE120221, GSE120446).

Massively parallel single cell RNA-sequencing—Single cells were encapsulated into emulsion droplets using Chromium Controller (10x Genomics). scRNA-seq libraries were constructed using Chromium Single Cell 3' v2 Reagent Kit according to the manufacturer's protocol. Briefly, post sorting sample volume was decreased and cells were examined under a microscope and counted with a hemocytometer. Cells were then loaded in each channel with a target output of ~4,000 cells. Reverse transcription and library preparation was done on C1000 Touch Thermal cycler with 96-Deep Well Reaction Module (Bio-Rad). Amplified cDNA and final libraries were evaluated on an Agilent BioAnalyzer using a High Sensitivity DNA Kit (Agilent Technologies). Individual libraries were diluted to 4nM and pooled for sequencing. Pools were sequenced with 75 cycle run kits (26bp Read1, 8bp Index1 and 55bp Read2) on the NextSeq 500 Sequencing System (Illumina) to ~70–80% saturation level.

Bulk RNA-sequencing—Bulk RNA sequencing libraries were prepared in accordance with the Smartseq2 protocol (Picelli et al., 2014). The libraries were sequenced on Illumina HiSeq 2500 and the resulting FASTQ files were aligned to the mouse genome (mm10, NCBI Build 38). Gene expression profile for the individual samples was thereafter calculated as RPKM values.

QUANTIFICATION AND STATISTICAL ANALYSIS

Quality control and preprocessing of single-cell RNA-seq data.—FASTQ files were processed with the CellRanger software (10x Genomics, Inc., version 2.0). Human genome hg19 was used as the reference genome (10x Genomics, Inc.) to generate the matrix files containing cell barcodes and transcript counts. Only cells with total UMI exceeding 600 were included in the downstream analysis. Statistics on the sequencing results are available in Table S1. Samples were initially analyzed using Pagoda2 (https://github.com/hms-dbmi/pagoda2) for quality control and data exploration.

Joint clustering and cell annotation—We used Conos (Barkas et al., 2019) (https://github.com/hms-dbmi/conos) to integrate multiple scRNA-seq datasets together and to align our data with other public scRNA-seq data, closely following the Conos tutorial. Sample pre-processing was performed using default pagoda2 settings ("basicP2proc()" function). The integration was performed using Conos with $k = 30$, $k_{self} = 15$, CPCA space, nPC=50, and n.odgenes=500, with an angular distance measure. Louvain clustering was used to build to determine joint cell clusters across the entire dataset collection. The annotation of clusters was performed manually based on the marker genes, with some clusters being assigned same label. One positioned between T and B lymphocytes was determined to represent doublets and was omitted from the analysis. As an additional check the annotation was compared with published scRNA-seq data from healthy BM (Oetjen et al., 2018). To do so, the raw count matrix was downloaded, and integrated into the joint graph using the same Conos settings. Conos label transfer was used to examine the correspondence of the annotation mapping. A 2D embedding (Fig. 1E) was generated using largeVis using default settings. To create a more detailed annotation of the T lymphocytes, we extracted all myeloid and all T cell populations (CD8+ T cells, CD4+ T cells, NK and NKT cells), and realigned separately using Conos. Leiden community detection method (as implemented in Conos) was used to determine refined joint clusters, providing higher resolution than the initial analysis. To

generate an embedding for the T cell populations (Fig. 6A), a largeVis embedding was first generated in 13 dimensions using default parameters, and then reduced to a 2D embedding using t-SNE (using default perplexity value of 50). Analogous procedure was performed for the myeloid cells, however the myeloid subpopulations were visualized using the original 2D embedding that was generated for the entire dataset (Fig. 1E).

Analysis of cell proportions and compositional data analysis—Statistical significance of proportion differences (Fig. 3A, S3A) was evaluated using Wilcoxon rank sum test, using 1000 bootstrap resampling rounds to report p-values at the 99% reproducibility power (*i.e.* reporting 0.99^{th} quantile of the sampled p-values). The p-values in the figures were reported using the following symbols: *p<0.05, **p<0.01, ***p<0.001, ****p<0.0001.

As an alternative to the simple proportion tests, we also used compositional data analysis (Pawlowsky-Glahn and Buccianti, 2011) to analyze the differences between Tumor/Involved and Benign samples (Fig. S3D). The CoDA avoids the non-independence of cell type fractions (in each sample they sum up to one). Isometric log-ratio (ilr) transformation was first applied, which allows to work with (n-1) independent artificial variables (ilr coordinates/variables) instead of cell type fractions constrained in the n-dimensional Simplex space. Each ilr variable is a linear combination of logarithms of cell type fractions. The set of (n-1) ilr coordinates forms the Euclidean space, where standard methods to discriminate groups of samples are permitted. To separate groups of samples (*e.g.,* Benign and Tumor) in the ilr-space, the canonical discriminant analysis was applied (using candisc package). The first canonical coordinate is a linear combination of log-fractions and represents a weighted contrast (balance) between cell types of positive and negative contributions to the linear combination. The loadings of different cell types on the first canonical coordinate were taken to be the separating coefficients (x axis, Fig. S3C). To evaluate the robustness and statistical significance of the separating coefficients, we performed random cell subsampling, repeating the procedure above 1000 sampling rounds. In each subsampling round, 500 cells were randomly sampled from each dataset to account for limited detection rates of cell types across datasets. Furthermore, to account for inter-patient variability, in each sampling round we performed bootstrap sampling of the datasets. Then the ilr calculation and subsequent procedures were repeated, and the separating coefficients resulting from different sampling rounds were shown on Fig. S3C as boxplots.

Analysis of expression distances—Expression differences between matching subpopulations (Fig. 3B, S3B) were determined by first estimating “mini-bulk” (or meta-cell) RNA-seq measurements for each subpopulation in each sample. Briefly, in each dataset, the molecules from all cells belonging to a given subpopulation were summed for each gene (*i.e.* forgetting cellular barcodes). The distance between the resulting high-coverage RNA-seq vectors was calculated using Jensen-Shannon divergence (JS). Expression distances between samples (Fig. 3B, S3B) were determined as a normalized weighted sum of JS divergence distances across all cell subpopulations contained in both samples, with the weight equal to the subpopulation proportion (measured as a minimal

proportion that the given cell subpopulation represents among the two samples being compared).

Cell-specific magnitude of expression shifts between sample fractions X and Y (e.g. Involved and Benign for Fig. 3C) for the individual cell types was determined as a difference of between-fraction distances and the mean within-fraction distance. Specifically, for samples i, j such that $i \in X$ and $j \in Y$, standardized distance $s_{ij} = d_{ij} - \frac{\sum_{k,l \in X} d_{kl} + \sum_{k,l \in Y} d_{kl}}{|x| + |Y|}$, where d_{ij} is the angular distance of the log-normalized mini-bulk molecule counts for the samples i and j. The boxplots in Fig. S3C show the s_{ij} values for the different classes of sample pairs. A minimal number of 10 cells (of the selected cell type) were required for a sample to be included in the comparison.

InferCNV analysis (Figure S2A)—To characterize copy number aberrations from the single cell RNA-seq data, inferCNV (Patel et al., 2014) (https://github.com/broadinstitute/inferCNV) was used. The raw count matrices for the measured tumor cells were extracted from the Conos object. For control cells, we have used normal epithelial prostate cells from three healthy prostate samples, published by Henry *et al.* (Henry et al., 2018). The count matrices for the control data were downloaded from GEO under the accession number GSE120716. For each of the three patients we randomly selected 300 epithelial cells to serve as a control. The following inferCNV parameters were used: denoise=TRUE, cutoff=0.1.

Analysis of intra-tumoral heterogeneity (Figures 2, S2)—Only samples with more than 10 annotated tumor cells were considered in the analysis. The datasets were normalized using pagoda2 (trim=0, min.n.odgenes=1000, nPcs=3). Size-normalized log counts were used for the projection, without taking into account the dataset-specific variance normalization. Tumor cell datasets were integrated using Conos (k=10, k.self=5, ncomps=10, metric='L2', n.odgenes=1000), and a joint largeVis embedding was obtained for visualization. Cell clusters were determined using Leiden community detection algorithm with resolution of 0.6.

Expression signature scores—To account for the complex gene expression patterns in M2 tumor associated macrophage, monocytes differentiation to macrophage, Treg activity, CD8+ T cell dysfunction and cytotoxicity, the signature scores were estimated as average expression values of the genes in a given set. Specifically, we first calculated signature score for each cell as an average normalized (for cell size) gene expression magnitudes, then the signature score for each sample was computed as the mean across all cells. All signature gene modules are listed in the Table S3. The M2 signature genes were from Aziz *et al.* (Azizi et al., 2018). CD8+ T cell cytotoxicity were measured by expression of CD8A, CD8B, GZMA, GZMM, GZMB, GZMK, GZMB, PRF1 (Rooney et al., 2015). The CD8+ T cell dysfunction genes were taken from Li *et al.* (Li et al., 2019). To define gene signature of monocytes to macrophage differentiation, we took top 100 differentially expressed genes based on published *in vitro* studies of monocytes to macrophage differentiation (Liu et al., 2008; Martinez et al., 2006). For this, the microarray data was analyzed by using affy (Liu et al., 2008) R package, and the differentially expressed genes were identified using limma (Martinez et al., 2006) R package. The statistical significance was assessed

using Wilcoxon rank-sum test. To ensure robustness of the result, two types of bootstrap resampling were performed: i) resampling cells, and ii) resampling genes. 1000 bootstrap resampling rounds were formed for each scenario, and a p-value corresponding to the 99% reproducibility power was reported in the figures using the following symbols: *p<0.05, **p<0.01, ***p<0.001, ****p<0.0001.

Differentially expressed genes—Differential expression (DE) and marker gene detection was performed using Wilcoxon rank sum test, implemented by the getDifferentialGenes() function from Conos R package. The genes were considered differentially expressed if the p-value determined Z score was greater than 3. Since the genes were used primarily for pathway enrichment analysis, the Z score was not corrected for multiple hypothesis testing. The getDifferentialGenes() function was used to identify differences between similar subpopulations (CTL-1 vs. CTL-2; Mono1 vs. Mono2 vs. Mono3).

For differential expression analysis between sample fractions (for example *Tumor* Treg vs. *Benign* Treg), getPerCellTypeDE() function in Conos was utilized. As described previously, it first forms “mini-bulk” (or meta-cell) RNA-seq measurements by combining all molecules measured for each gene in each subpopulation in each sample. This results in a collection of bulk-like RNA-seq samples, and the differential expression problem is then reformulated as a standard bulk RNA-seq differential expression problem DESeq2 to compare these “bulk-like” meta-cell samples, using appropriate design models (i.e. *Tumor* vs. *Benign* factor on samples). This approach is suitable for the comping groups of patient samples, as it focuses on the inter-individual variability (variability between patients) as opposed to cell-to-cell variability within each sample which is much smaller. At the same time, the overall depth of the “mini-bulk” profiles enable to estimate the uncertainty of each the expression magnitudes (*i.e.* the samples with large number of cells will result in mini-bulk profiles of greater depth). Preliminary benchmarking shows that such ‘mini-bulk’ approach is effective for differential expression testing (Crowell et al., 2020) . A minimal number of 10 cells (of the selected cell type) were required for a sample to be included in the comparison. The DESeq2 analyses were ran using “~fraction” model. For paired tests (within individual), “~patient+fraction” model was used. The p-values were translated into Z scores, with positive scores corresponding to upregulation, negative to downregulation. Several additional tests were implemented in additional to the mini-bulk based tests described above: i) a Wilcoxon rank sum test across mini-bulk samples (wZ); ii) Wilcoxon rank sum test on samples with cells resampled using bootstrap sampling (100 sampling rounds), reporting the Z score at 90% reproducibility power (bwZ); and iii) Wilcoxon rank sum test across single-cell expression matrix (i.e. without collapsing cells into “mini-bulk” samples) (cwZ). These tests are included in the interactive differential expression tables on the author’s website.

Comparative analysis with public cancer datasets (Figure 5)—To compare the profile of myeloid and T lymphocyte populations observed in our BM study with the immune microenvironment of other cancer types, we used *Conos* (with $k = 30$, $k_{self} = 10$ CPCA rotation space and an angular distance measure) to perform a joint alignment of

myeloid cells from benign BM (Oetjen et al., 2018), PCa bone metastases, pancreatic cancer, lung cancer (Lambrechts et al., 2018) and liver cancer (Zhang et al., 2019) samples. Bone marrow cell annotations were propagated to other cancer types using *propagateLabels()* function in *Conos*. For myeloid cells, we measured the cell proportion of TIM and TAM across cancer types, compared monocyte inflammatory signature score for the TIM-like cells, and the M2 macrophage score for the TAM-like. Select marker genes were shown in the heatmaps (Fig. 5D,E). For comparison of the T lymphocyte states, only study containing matched (adjacent) normal control samples were analyzed. Joint alignment and label propagation were then performed in the same way as for monocytes. We then evaluated T cells exhaustion scores in CTLs, observing the expected increase in exhaustion signature between the tumor and adjacent normal samples, despite variable base-level expression level of between the tissues (Fig. S5G).

Ligand and Receptor analysis (Figure 6H,I)—To screen for potential channels of communications between different cell types, we looked at expression of previously annotated reciprocal ligand-receptor pairs. The annotated list containing 1307 pairs of well-annotated receptors and ligands was downloaded from CellPhoneDB (Vento-Tormo et al., 2018). Both ligands and corresponding receptors were required to be detected in more than 10% of the cells of a given type. Initial filtering reveled 241 ligand-receptor pairs between myeloid cell and T cells. (Fig. 6H, Table S4). Further filtering for ligand-receptor channels potentially connecting TIM/TAM with T cell populations was performed by requiring ligands to be upregulated in TIM or TAM cells (compared to other myeloid cells, Zscore >5), and requiring the corresponding receptor to be upregulated (log fold change >0) in T cells in *Tumor* compared to *Benign* (Table S4). Differentially expressed genes were identified using Wilcoxon rank sum test, implemented by the getDifferentialGenes function in Conos.

Survival analysis on bulk data (Figure S4E)—To test if a given gene signature is associated with differential survival of cancer patients (Cancer Genome Atlas Research et al., 2013) (Fig. S4E), we first calculated average expression of the signature in each cancer type based on the bulk RNA-seq data. The bulk patient samples were then stratified into two groups, based on average signature expression, separating patients with top 25% of scores and bottom 25%. A standard Kaplan-Meier survival analysis was then used to determine the association of these groups with survival rate. Kaplan-Meier survival analysis in Fig. 7B,C and Fig. S4E were performed using the *survival* R package.

Gene ontology and gene set enrichment analysis (Figures 3D,E S3F,G)— *clusterProfiler* package was used to evaluate enrichment of the GO BP categories in the sets of top 300 up- and down-regulated genes separately(Wu et al., 2021). The set of all expressed genes was used as a background. The categories with adjusted p-value of enrichment below 0.05 were then clustered into 20 clusters based on the similarity of the participating genes (*i.e.* the genes out of the 300 genes being tested that fall within each category, using binary distance measure). The clusters were named according to the most significantly enriched category, shortening some names to fit the plot.

Supplementary Material

Refer to Web version on PubMed Central for supplementary material.

Acknowledgements

We gratefully acknowledge support from Bill & Cheryl Swanson, Gunther & Maggie Buerman and the Cygnus Montanus Foundation founded by the Svanberg family. We acknowledge funding from NIH CA193481, DK103074 (DTS and PVK), NCI CA163191 (DTS), HL131768 (PVK), Dana-Farber/ Harvard Cancer Center Nodal Award (CCSG grant P30CA006516), the Harvard Ludwig Cancer Center, the Harvard Stem Cell Institute and the Gerald and Darlene Jordan Professor of Medicine Chair (DTS). N.B and K.G were funded by the Swedish Research Council. N.S received the AACR-Millennium Fellowship in PCa Research. Y.K was supported by a grant from the STARR cancer consortium. We thank Carl A Power for generously donating the murine RM1-BoM1 cell line. Olga Kharchenko designed illustrations in Figure 1A and the graphical abstract. We thank Dr. Chin-Lee Wu and Dr. Shulin Wu from the Pathology Department at Massachusetts General Hospital for providing the H&E images in Figure 1B/S1A. We thank the Center for Skeletal Research at Massachusetts General Hospital, supported by a grant from NIAMS (P30 AR075042) at NIH.

References

Azizi E, Carr AJ, Plitas G, Cornish AE, Konopacki C, Prabhakaran S, Nainys J, Wu K, Kiseliovas V, Setty M, et al. (2018). Single-Cell Map of Diverse Immune Phenotypes in the Breast Tumor Microenvironment. Cell 174, 1293–1308 e1236. [PubMed: 29961579]

Bachelder RE, Wendt MA, and Mercurio AM (2002). Vascular endothelial growth factor promotes breast carcinoma invasion in an autocrine manner by regulating the chemokine receptor CXCR4. Cancer research 62, 7203–7206. [PubMed: 12499259]

Barkas N, Petukhov V, Nikolaeva D, Lozinsky Y, Demharter S, Khodosevich K, and Kharchenko PV (2019). Joint analysis of heterogeneous single-cell RNA-seq dataset collections. Nature methods 16, 695–698. [PubMed: 31308548]

Becking K, Haarman BC, van der Lek RF, Grosse L, Nolen WA, Claes S, Drexhage HA, and Schoevers RA (2015). Inflammatory monocyte gene expression: trait or state marker in bipolar disorder? International journal of bipolar disorders 3, 20. [PubMed: 26381439]

Beer TM, Kwon ED, Drake CG, Fizazi K, Logothetis C, Gravis G, Ganju V, Polikoff J, Saad F, Humanski P, et al. (2017). Randomized, Double-Blind, Phase III Trial of Ipilimumab Versus Placebo in Asymptomatic or Minimally Symptomatic Patients With Metastatic Chemotherapy-Naive Castration-Resistant Prostate Cancer. Journal of clinical oncology : official journal of the American Society of Clinical Oncology 35, 40–47. [PubMed: 28034081]

Beider K, Abraham M, Begin M, Wald H, Weiss ID, Wald O, Pikarsky E, Abramovitch R, Zeira E, Galun E, et al. (2009). Interaction between CXCR4 and CCL20 pathways regulates tumor growth. PloS one 4, e5125. [PubMed: 19340288]

Bilir B, Osunkoya AO, Wiles W. G. t., Sannigrahi S, Lefebvre V, Metzger D, Spyropoulos DD, Martin WD, and Moreno CS (2016). SOX4 Is Essential for Prostate Tumorigenesis Initiated by PTEN Ablation. Cancer research 76, 1112–1121. [PubMed: 26701805]

Bouma G, Zamuner S, Hicks K, Want A, Oliveira J, Choudhury A, Brett S, Robertson D, Felton L, Norris V, et al. (2017). CCL20 neutralization by a monoclonal antibody in healthy subjects selectively inhibits recruitment of CCR6(+) cells in an experimental suction blister. British journal of clinical pharmacology 83, 1976–1990. [PubMed: 28295451]

Cancer Genome Atlas Research, N., Weinstein JN, Collisson EA, Mills GB, Shaw KR, Ozenberger BA, Ellrott K, Shmulevich I, Sander C, and Stuart JM (2013). The Cancer Genome Atlas Pan-Cancer analysis project. Nature genetics 45, 1113–1120. [PubMed: 24071849]

Chen J, Cheung F, Shi R, Zhou H, Lu W, and Consortium CHI (2018). PBMC fixation and processing for Chromium single-cell RNA sequencing. Journal of translational medicine 16, 198. [PubMed: 30016977]

Chen S, Zhu G, Yang Y, Wang F, Xiao YT, Zhang N, Bian X, Zhu Y, Yu Y, Liu F, et al. (2021). Single-cell analysis reveals transcriptomic remodellings in distinct cell types that contribute to human prostate cancer progression. Nature cell biology 23, 87–98. [PubMed: 33420488]

Coffelt SB, Wellenstein MD, and de Visser KE (2016). Neutrophils in cancer: neutral no more. Nature reviews Cancer 16, 431–446. [PubMed: 27282249]

Crowell HL, Soneson C, Germain PL, Calini D, Collin L, Raposo C, Malhotra D, and Robinson MD (2020). muscat detects subpopulation-specific state transitions from multi-sample multi-condition single-cell transcriptomics data. Nature communications 11, 6077.

de Bono JS, Logothetis CJ, Molina A, Fizazi K, North S, Chu L, Chi KN, Jones RJ, Goodman OB Jr., Saad F, et al. (2011). Abiraterone and increased survival in metastatic prostate cancer. The New England journal of medicine 364, 1995–2005. [PubMed: 21612468]

de Bono JS, Oudard S, Ozguroglu M, Hansen S, Machiels JP, Kocak I, Gravis G, Bodrogi I, Mackenzie MJ, Shen L, et al. (2010). Prednisone plus cabazitaxel or mitoxantrone for metastatic castration-resistant prostate cancer progressing after docetaxel treatment: a randomised open-label trial. Lancet 376, 1147–1154. [PubMed: 20888992]

De Palma M, and Lewis CE (2013). Macrophage regulation of tumor responses to anticancer therapies. Cancer cell 23, 277–286. [PubMed: 23518347]

DeNardo DG, and Ruffell B (2019). Macrophages as regulators of tumour immunity and immunotherapy. Nature reviews Immunology 19, 369–382.

Ding J, Adiconis X, Simmons SK, Kowalczyk MS, Hession CC, Marjanovic ND, Hughes TK, Wadsworth MH, Burks T, Nguyen LT, et al. (2020). Systematic comparison of single-cell and single-nucleus RNA-sequencing methods. Nature biotechnology 38, 737–746.

Efremova M, Vento-Tormo M, Teichmann SA, and Vento-Tormo R (2020). CellPhoneDB: inferring cell-cell communication from combined expression of multi-subunit ligand-receptor complexes. Nature protocols 15, 1484–1506. [PubMed: 32103204]

Engblom C, Pfirschke C, and Pittet MJ (2016). The role of myeloid cells in cancer therapies. Nature reviews Cancer 16, 447–462. [PubMed: 27339708]

Fergusson JR, Huhn MH, Swadling L, Walker LJ, Kurioka A, Llibre A, Bertoletti A, Hollander G, Newell EW, Davis MM, et al. (2016). CD161(int)CD8+ T cells: a novel population of highly functional, memory CD8+ T cells enriched within the gut. Mucosal immunology 9, 401–413. [PubMed: 26220166]

Getschman AE, Imai Y, Larsen O, Peterson FC, Wu X, Rosenkilde MM, Hwang ST, and Volkman BF (2017). Protein engineering of the chemokine CCL20 prevents psoriasiform dermatitis in an IL-23-dependent murine model. Proceedings of the National Academy of Sciences of the United States of America 114, 12460–12465. [PubMed: 29109267]

Glatman Zaretsky A, Konradt C, Depis F, Wing JB, Goenka R, Atria DG, Silver JS, Cho S, Wolf AI, Quinn WJ, et al. (2017). T Regulatory Cells Support Plasma Cell Populations in the Bone Marrow. Cell reports 18, 1906–1916. [PubMed: 28228257]

Goswami S, Aparicio A, and Subudhi SK (2016). Immune Checkpoint Therapies in Prostate Cancer. Cancer J 22, 117–120. [PubMed: 27111907]

Halabi S, Kelly WK, Ma H, Zhou H, Solomon NC, Fizazi K, Tangen CM, Rosenthal M, Petrylak DP, Hussain M, et al. (2016). Meta-Analysis Evaluating the Impact of Site of Metastases on Overall Survival in Men With Castration-Resistant Prostate Cancer. Journal of clinical oncology : official journal of the American Society of Clinical Oncology 34, 1652–1659. [PubMed: 26951312]

He MX, Cuoco MS, Crowdis J, Bosma-Moody A, Zhang Z, Bi K, Kanodia A, Su MJ, Ku SY, Garcia MM, et al. (2021). Transcriptional mediators of treatment resistance in lethal prostate cancer. Nature medicine 27, 426–433.

Henry GH, Malewska A, Joseph DB, Malladi VS, Lee J, Torrealba J, Mauck RJ, Gahan JC, Raj GV, Roehrborn CG, et al. (2018). A Cellular Anatomy of the Normal Adult Human Prostate and Prostatic Urethra. Cell reports 25, 3530–3542 e3535. [PubMed: 30566875]

Hippe A, Braun SA, Olah P, Gerber PA, Schorr A, Seeliger S, Holtz S, Jannasch K, Pivarcsi A, Buhren B, et al. (2020). EGFR/Ras-induced CCL20 production modulates the tumour microenvironment. British journal of cancer 123, 942–954. [PubMed: 32601464]

Huynh J, Etemadi N, Hollande F, Ernst M, and Buchert M (2017). The JAK/STAT3 axis: A comprehensive drug target for solid malignancies. Seminars in cancer biology 45, 13–22. [PubMed: 28647610]

Hyakusoku H, Sano D, Takahashi H, Hatano T, Isono Y, Shimada S, Ito Y, Myers JN, and Oridate N (2016). JunB promotes cell invasion, migration and distant metastases of head and neck squamous cell carcinoma. Journal of experimental & clinical cancer research : CR 35, 6. [PubMed: 26754630]

Ikeda S, Kitadate A, Ito M, Abe F, Nara M, Watanabe A, Takahashi N, Miyagaki T, Sugaya M, and Tagawa H (2016). Disruption of CCL20-CCR6 interaction inhibits metastases of advanced cutaneous T-cell lymphoma. Oncotarget 7, 13563–13574. [PubMed: 26789110]

Ito M, Teshima K, Ikeda S, Kitadate A, Watanabe A, Nara M, Yamashita J, Ohshima K, Sawada K, and Tagawa H (2014). MicroRNA-150 inhibits tumor invasion and metastases by targeting the chemokine receptor CCR6, in advanced cutaneous T-cell lymphoma. Blood 123, 1499–1511. [PubMed: 24385540]

Jiao S, Subudhi SK, Aparicio A, Ge Z, Guan B, Miura Y, and Sharma P (2019). Differences in Tumor Microenvironment Dictate T Helper Lineage Polarization and Response to Immune Checkpoint Therapy. Cell 179, 1177–1190 e1113. [PubMed: 31730856]

Kakhki VR, Anvari K, Sadeghi R, Mahmoudian AS, and Torabian-Kakhki M (2013). Pattern and distribution of bone metastases in common malignant tumors. Nucl Med Rev Cent East Eur 16, 66–69. [PubMed: 24068635]

Laccetti AL, and Subudhi SK (2017). Immunotherapy for metastatic prostate cancer: immuno-cold or the tip of the iceberg? Current opinion in urology 27, 566–571. [PubMed: 28825923]

Laffan SB, Thomson AS, Mai S, Fishman C, Kambara T, Nistala K, Raymond JT, Chen S, Ramani T, Pageon L, et al. (2020). Immune complex disease in a chronic monkey study with a humanised, therapeutic antibody against CCL20 is associated with complement-containing drug aggregates. PloS one 15, e0231655. [PubMed: 32325480]

Lambrechts D, Wauters E, Boeckx B, Aibar S, Nittner D, Burton O, Bassez A, Decaluwe H, Pircher A, Van den Eynde K, et al. (2018). Phenotype molding of stromal cells in the lung tumor microenvironment. Nature medicine 24, 1277–1289.

Landi L, D'Inca F, Gelibter A, Chiari R, Grossi F, Delmonte A, Passaro A, Signorelli D, Gelsomino F, Galetta D, et al. (2019). Bone metastases and immunotherapy in patients with advanced non-small-cell lung cancer. Journal for immunotherapy of cancer 7, 316. [PubMed: 31752994]

Lawrence T (2009). The nuclear factor NF-kappaB pathway in inflammation. Cold Spring Harbor perspectives in biology 1, a001651. [PubMed: 20457564]

Lee PP, Yee C, Savage PA, Fong L, Brockstedt D, Weber JS, Johnson D, Swetter S, Thompson J, Greenberg PD, et al. (1999). Characterization of circulating T cells specific for tumor-associated antigens in melanoma patients. Nature medicine 5, 677–685.

Lee SK, Park KK, Kim HJ, Park J, Son SH, Kim KR, and Chung WY (2017). Human antigen R-regulated CCL20 contributes to osteolytic breast cancer bone metastases. Scientific reports 7, 9610. [PubMed: 28851919]

Lewis CE, Harney AS, and Pollard JW (2016). The Multifaceted Role of Perivascular Macrophages in Tumors. Cancer cell 30, 365. [PubMed: 27505682]

Li H, van der Leun AM, Yofe I, Lubling Y, Gelbard-Solodkin D, van Akkooi ACJ, van den Braber M, Rozeman EA, Haanen J, Blank CU, et al. (2019). Dysfunctional CD8 T Cells Form a Proliferative, Dynamically Regulated Compartment within Human Melanoma. Cell 176, 775–789 e718. [PubMed: 30595452]

Liu H, Shi B, Huang CC, Eksarko P, and Pope RM (2008). Transcriptional diversity during monocyte to macrophage differentiation. Immunology letters 117, 70–80. [PubMed: 18276018]

Lu E, Su J, Zhou Y, Zhang C, and Wang Y (2017). CCL20/CCR6 promotes cell proliferation and metastases in laryngeal cancer by activating p38 pathway. Biomedicine & pharmacotherapy = Biomedecine & pharmacotherapie 85, 486–492. [PubMed: 27916417]

Mantovani A, Marchesi F, Malesci A, Laghi L, and Allavena P (2017). Tumour-associated macrophages as treatment targets in oncology. Nat Rev Clin Oncol 14, 399–416. [PubMed: 28117416]

Martinez FO, Gordon S, Locati M, and Mantovani A (2006). Transcriptional profiling of the human monocyte-to-macrophage differentiation and polarization: new molecules and patterns of gene expression. Journal of immunology 177, 7303–7311.

Melaiu O, Lucarini V, Cifaldi L, and Fruci D (2019). Influence of the Tumor Microenvironment on NK Cell Function in Solid Tumors. Frontiers in immunology 10, 3038. [PubMed: 32038612]

Merchant N, Nagaraju GP, Rajitha B, Lammata S, Jella KK, Buchwald ZS, Lakka SS, and Ali AN (2017). Matrix metalloproteinases: their functional role in lung cancer. Carcinogenesis 38, 766–780. [PubMed: 28637319]

Mereu E, Lafzi A, Moutinho C, Ziegenhain C, McCarthy DJ, Alvarez-Varela A, Batlle E, Sagar, Grun D, Lau JK, et al. (2020). Benchmarking single-cell RNA-sequencing protocols for cell atlas projects. Nature biotechnology 38, 747–755.

Munn DH, and Bronte V (2016). Immune suppressive mechanisms in the tumor microenvironment. Current opinion in immunology 39, 1–6. [PubMed: 26609943]

Neeb A, Wallbaum S, Novac N, Dukovic-Schulze S, Scholl I, Schreiber C, Schlag P, Moll J, Stein U, and Sleeman JP (2012). The immediate early gene Ier2 promotes tumor cell motility and metastases, and predicts poor survival of colorectal cancer patients. Oncogene 31, 3796–3806. [PubMed: 22120713]

Nunamaker EA, Artwohl JE, Anderson RJ, and Fortman JD (2013). Endpoint refinement for total body irradiation of C57BL/6 mice. Comparative medicine 63, 22–28. [PubMed: 23561934]

Oetjen KA, Lindblad KE, Goswami M, Gui G, Dagur PK, Lai C, Dillon LW, McCoy JP, and Hourigan CS (2018). Human bone marrow assessment by single-cell RNA sequencing, mass cytometry, and flow cytometry. JCI insight 3.

Parker C, Nilsson S, Heinrich D, Helle SI, O'Sullivan JM, Fossa SD, Chodacki A, Wiechno P, Logue J, Seke M, et al. (2013). Alpha emitter radium-223 and survival in metastatic prostate cancer. The New England journal of medicine 369, 213–223. [PubMed: 23863050]

Patel AP, Tirosh I, Trombetta JJ, Shalek AK, Gillespie SM, Wakimoto H, Cahill DP, Nahed BV, Curry WT, Martuza RL, et al. (2014). Single-cell RNA-seq highlights intratumoral heterogeneity in primary glioblastoma. Science 344, 1396–1401. [PubMed: 24925914]

Pawlowsky-Glahn V, and Buccianti A (2011). Compositional Data Analysis: Theory and Applications. John Wiley & Sons, Ltd.

Pellikainen JM, Ropponen KM, Kataja VV, Kellokoski JK, Eskelinen MJ, and Kosma VM (2004). Expression of matrix metalloproteinase (MMP)-2 and MMP-9 in breast cancer with a special reference to activator protein-2, HER2, and prognosis. Clinical cancer research : an official journal of the American Association for Cancer Research 10, 7621–7628.

Peng J, Sun BF, Chen CY, Zhou JY, Chen YS, Chen H, Liu L, Huang D, Jiang J, Cui GS, et al. (2019). Single-cell RNA-seq highlights intra-tumoral heterogeneity and malignant progression in pancreatic ductal adenocarcinoma. Cell research 29, 725–738. [PubMed: 31273297]

Petrylak DP, Tangen CM, Hussain MH, Lara PN Jr., Jones JA, Taplin ME, Burch PA, Berry D, Moinpour C, Kohli M, et al. (2004). Docetaxel and estramustine compared with mitoxantrone and prednisone for advanced refractory prostate cancer. The New England journal of medicine 351, 1513–1520. [PubMed: 15470214]

Picelli S, Faridani OR, Bjorklund AK, Winberg G, Sagasser S, and Sandberg R (2014). Full-length RNA-seq from single cells using Smart-seq2. Nature protocols 9, 171–181. [PubMed: 24385147]

Picker LJ, Treer JR, Ferguson-Darnell B, Collins PA, Buck D, and Terstappen LW (1993). Control of lymphocyte recirculation in man. I. Differential regulation of the peripheral lymph node homing receptor L-selectin on T cells during the virgin to memory cell transition. Journal of immunology 150, 1105–1121.

Power CA, Pwint H, Chan J, Cho J, Yu Y, Walsh W, and Russell PJ (2009). A novel model of bone-metastatic prostate cancer in immunocompetent mice. The Prostate 69, 1613–1623. [PubMed: 19585491]

Ranasinghe R, and Eri R (2018). Modulation of the CCR6-CCL20 Axis: A Potential Therapeutic Target in Inflammation and Cancer. Medicina (Kaunas) 54.

Robert R, Ang C, Sun G, Juglair L, Lim EX, Mason LJ, Payne NL, Bernard CC, and Mackay CR (2017). Essential role for CCR6 in certain inflammatory diseases demonstrated using specific antagonist and knockin mice. JCI insight 2.

Rooney MS, Shukla SA, Wu CJ, Getz G, and Hacohen N (2015). Molecular and genetic properties of tumors associated with local immune cytolytic activity. Cell 160, 48–61. [PubMed: 25594174]

Saad F, Gleason DM, Murray R, Tchekmedyian S, Venner P, Lacombe L, Chin JL, Vinholes JJ, Goas JA, Zheng M, and Zoledronic Acid Prostate Cancer Study, G. (2004). Long-term efficacy of zoledronic acid for the prevention of skeletal complications in patients with metastatic hormone-refractory prostate cancer. Journal of the National Cancer Institute 96, 879–882. [PubMed: 15173273]

Sanjabi S, Zenewicz LA, Kamanaka M, and Flavell RA (2009). Anti-inflammatory and pro-inflammatory roles of TGF-beta, IL-10, and IL-22 in immunity and autoimmunity. Current opinion in pharmacology 9, 447–453. [PubMed: 19481975]

Smillie CS, Biton M, Ordovas-Montanes J, Sullivan KM, Burgin G, Graham DB, Herbst RH, Rogel N, Slyper M, Waldman J, et al. (2019). Intra- and Inter-cellular Rewiring of the Human Colon during Ulcerative Colitis. Cell 178, 714–730 e722. [PubMed: 31348891]

Tannock IF, de Wit R, Berry WR, Horti J, Pluzanska A, Chi KN, Oudard S, Theodore C, James ND, Turesson I, et al. (2004). Docetaxel plus prednisone or mitoxantrone plus prednisone for advanced prostate cancer. The New England journal of medicine 351, 1502–1512. [PubMed: 15470213]

Thompson TC, Southgate J, Kitchener G, and Land H (1989). Multistage carcinogenesis induced by ras and myc oncogenes in a reconstituted organ. Cell 56, 917–930. [PubMed: 2538247]

Tirosh I, Izar B, Prakadan SM, Wadsworth MH 2nd, Treacy D, Trombetta JJ, Rotem A, Rodman C, Lian C, Murphy G, et al. (2016). Dissecting the multicellular ecosystem of metastatic melanoma by single-cell RNA-seq. Science 352, 189–196. [PubMed: 27124452]

Tiwari N, Tiwari VK, Waldmeier L, Balwierz PJ, Arnold P, Pachkov M, Meyer-Schaller N, Schubeler D, van Nimwegen E, and Christofori G (2013). Sox4 is a master regulator of epithelial-mesenchymal transition by controlling Ezh2 expression and epigenetic reprogramming. Cancer cell 23, 768–783. [PubMed: 23764001]

Vento-Tormo R, Efremova M, Botting RA, Turco MY, Vento-Tormo M, Meyer KB, Park JE, Stephenson E, Polanski K, Goncalves A, et al. (2018). Single-cell reconstruction of the early maternal-fetal interface in humans. Nature 563, 347–353. [PubMed: 30429548]

Vlaicu P, Mertins P, Mayr T, Widschwendter P, Ataseven B, Hogel B, Eiermann W, Knyazev P, and Ullrich A (2013). Monocytes/macrophages support mammary tumor invasivity by co-secreting lineage-specific EGFR ligands and a STAT3 activator. BMC cancer 13, 197. [PubMed: 23597096]

Walch-Ruckheim B, Mavrova R, Henning M, Vicinus B, Kim YJ, Bohle RM, Juhasz-Boss I, Solomayer EF, and Smola S (2015). Stromal Fibroblasts Induce CCL20 through IL6/C/EBPbeta to Support the Recruitment of Th17 Cells during Cervical Cancer Progression. Cancer research 75, 52485259.

Wang D, Yang L, Yu W, Wu Q, Lian J, Li F, Liu S, Li A, He Z, Liu J, et al. (2019). Colorectal cancer cell-derived CCL20 recruits regulatory T cells to promote chemoresistance via FOXO1/CEBPB/NF-kappaB signaling. Journal for immunotherapy of cancer 7, 215. [PubMed: 31395078]

Wang X, He Y, Zhang Q, Ren X, and Zhang Z (2021). Direct Comparative Analyses of 10X Genomics Chromium and Smart-seq2. Genomics Proteomics Bioinformatics.

Willinger T, Freeman T, Herbert M, Hasegawa H, McMichael AJ, and Callan MF (2006). Human naive CD8 T cells down-regulate expression of the WNT pathway transcription factors lymphoid enhancer binding factor 1 and transcription factor 7 (T cell factor-1) following antigen encounter in vitro and in vivo. Journal of immunology 176, 1439–1446.

Witkowski MT, Dolgalev I, Evensen NA, Ma C, Chambers T, Roberts KG, Sreeram S, Dai Y, Tikhonova AN, Lasry A, et al. (2020). Extensive Remodeling of the Immune Microenvironment in B Cell Acute Lymphoblastic Leukemia. Cancer cell 37, 867–882 e812. [PubMed: 32470390]

Woo EY, Yeh H, Chu CS, Schlienger K, Carroll RG, Riley JL, Kaiser LR, and June CH (2002). Cutting edge: Regulatory T cells from lung cancer patients directly inhibit autologous T cell proliferation. Journal of immunology 168, 4272–4276.

Xiang L, and Gilkes DM (2019). The Contribution of the Immune System in Bone Metastases Pathogenesis. International journal of molecular sciences 20.

Xiong D, Wang Y, and You M (2020). A gene expression signature of TREM2(hi) macrophages and gammadelta T cells predicts immunotherapy response. Nature communications 11, 5084.

Zhang L, Yu X, Zheng L, Zhang Y, Li Y, Fang Q, Gao R, Kang B, Zhang Q, Huang JY, et al. (2018). Lineage tracking reveals dynamic relationships of T cells in colorectal cancer. Nature 564, 268–272. [PubMed: 30479382]

Zhang Q, He Y, Luo N, Patel SJ, Han Y, Gao R, Modak M, Carotta S, Haslinger C, Kind D, et al. (2019). Landscape and Dynamics of Single Immune Cells in Hepatocellular Carcinoma. Cell 179, 829–845 e820. [PubMed: 31675496]

Zou L, Barnett B, Safah H, Larussa VF, Evdemon-Hogan M, Mottram P, Wei S, David O, Curiel TJ, and Zou W (2004). Bone marrow is a reservoir for CD4+CD25+ regulatory T cells that traffic through CXCL12/CXCR4 signals. Cancer research 64, 8451–8455. [PubMed: 15548717]

Wu T, Hu E, Xu S, Chen M, Guo P, Dai Z, Feng T, Zhou L, Tang W, Zhan L, et al. (2021). clusterProfiler 4.0: A universal enrichment tool for interpreting omics data. Innovations 2.

Highlights

- An immune-suppressive microenvironment characterizes bone metastatic prostate cancer.
- Infiltrating T cells are exhausted and dysfunctional.
- Inflammatory monocytes and M2 polarized macrophages are enriched and overexpress CCL20
- Disruption of the CCL20/CCR6 axes relieves T cell exhaustion and extends survival

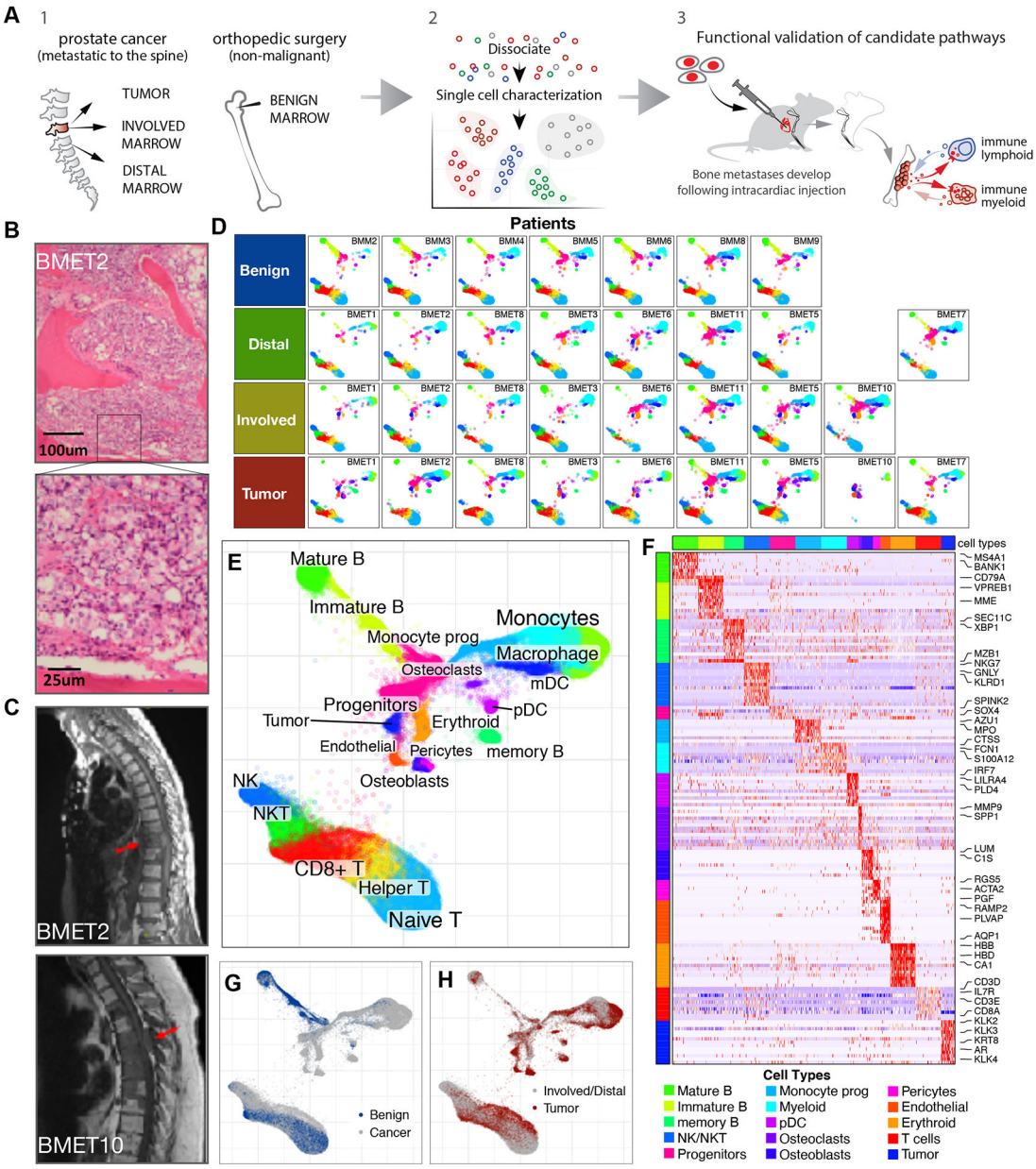

Figure 1. Transcriptional impact of PCa metastases on the BM.

(A) Schematic illustration of study design.

(B) H&E-stained tissue sections of metastatic tumor from a representative patient with bone metastatic PCa (100x -top, 400x -bottom).

(C) Sagittal T1 MRI imaging of the thoracic spine for each of those three cases showing tumor masses with spinal cord compression. (top) The T10 vertebral body (arrow) is structurally compromised by tumor. (*bottom*) An extradural tumor mass in the dorsal spinal canal at the T5 level (arrow).

(D,E) The analysis integrates scRNA-seq from three fractions (Tumor, Involved, Distal) of 9 metastatic PCa patients (rows), and 7 Benign BM controls. The datasets were integrated to

establish joint embedding and annotation (E). Projections of individual samples are shown in D.

(F) Marker genes for major cell populations.

(G) The difference in frequency of major subpopulations between Benign controls and cancer patients (all three fractions).

(H) Compositional differences between Tumor and Involved/Distal fractions.

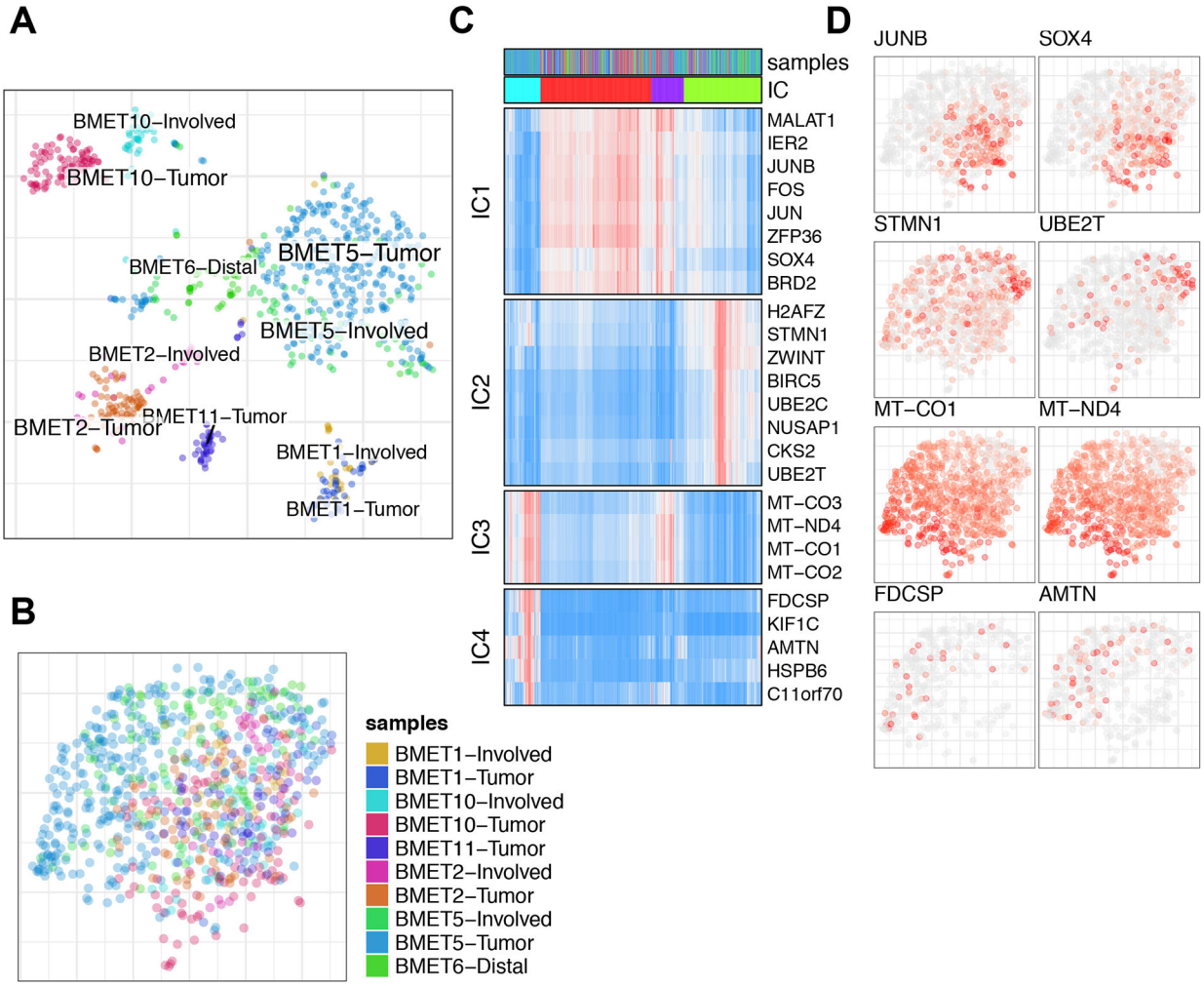

Figure 2. Common axes of intratumoral heterogeneity are seen within the metastatic tumor populations.

(A) Transcriptional heterogeneity of tumor cells from different samples is visualized on a tSNE embedding.

(B) Integration of tumor cells from different patients using Conos (same colors as in A).

(C) Expression of high-loading genes for four independent components (ICs) is shown based on the ICA analysis of the integrated tumor cell populations, illustrating re-current aspects of transcriptional heterogeneity between patients (red -high expression; blue -low).

(D) Expression of high-loading genes identified by ICA are shown on the combined Conos embedding B.

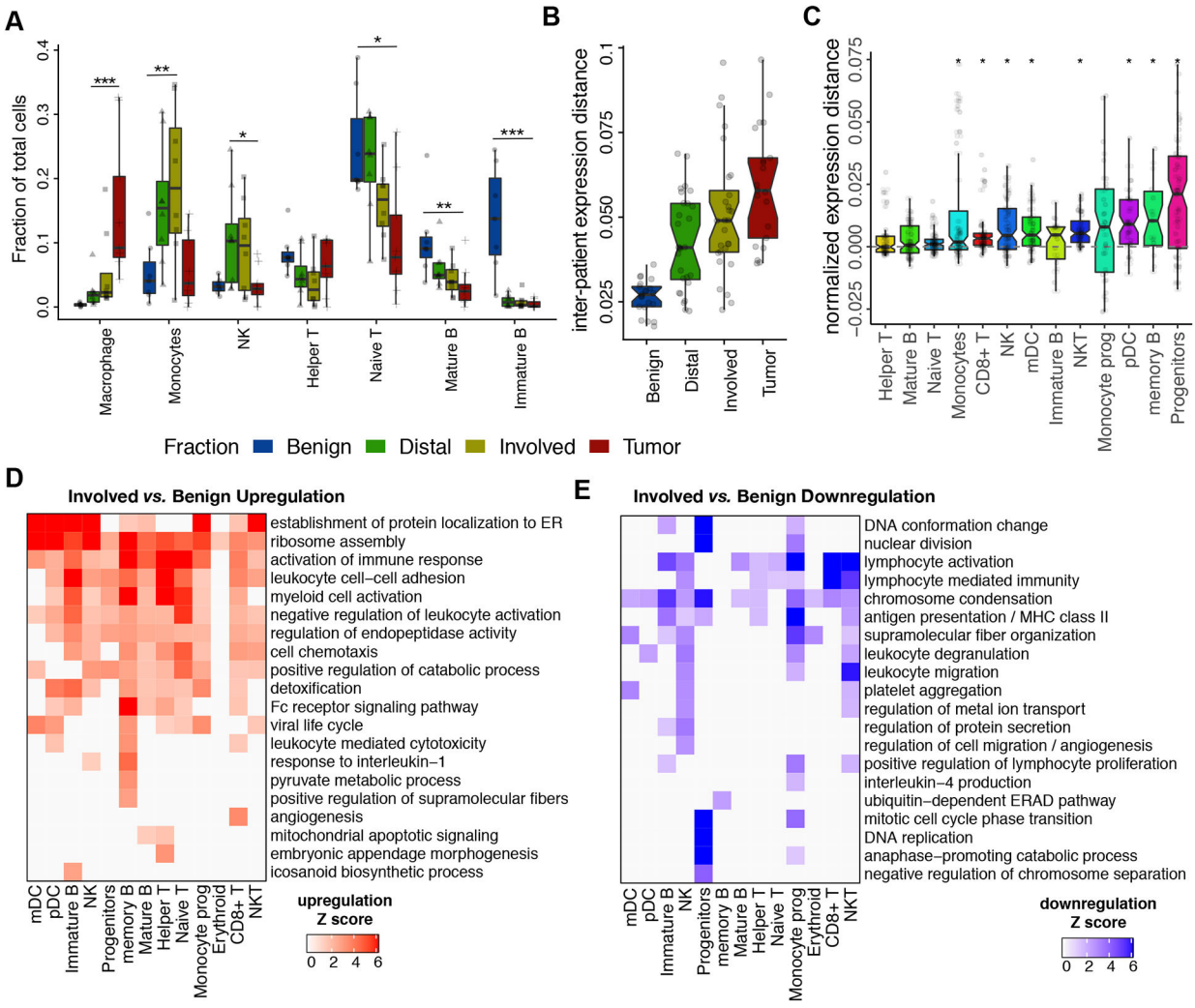

Figure 3. Overview of compositional and transcriptional shifts associated with presence of metastases in the BM.

(A) Compositional shifts for the most affected cell types are shown as boxplots comparing proportion of major cell populations between Benign controls and different cancer fractions (see Fig. S3A for all populations). (*p<0.05, ****p<0.0001) for select pairs, based on a Wilcoxon rank sum test.

(B) Average combined expression distances between different patients.

(C) The boxplots show normalized expression distances (y axis) show the extent of transcriptional variation between Involved and Benign fractions relative to expression variation within the fractions. Significance is shown based on empirical randomization of sample group assignment. Boxplots in A-C include centerline(median), 25th to 75th percentiles; and whiskers are highest and lowest values no greater than 1.5x interquartile range.

(D,E) Overview of the GO BP category enrichment in the top 300 up-regulated (D) and down-regulated (E) genes in the Involved *vs.* Benign differential expression analysis performed for each major cell subpopulation. Gene sets showing significant enrichment

(FDR <0.05) were clustered into 20 clusters according to the similarity of the participating genes.

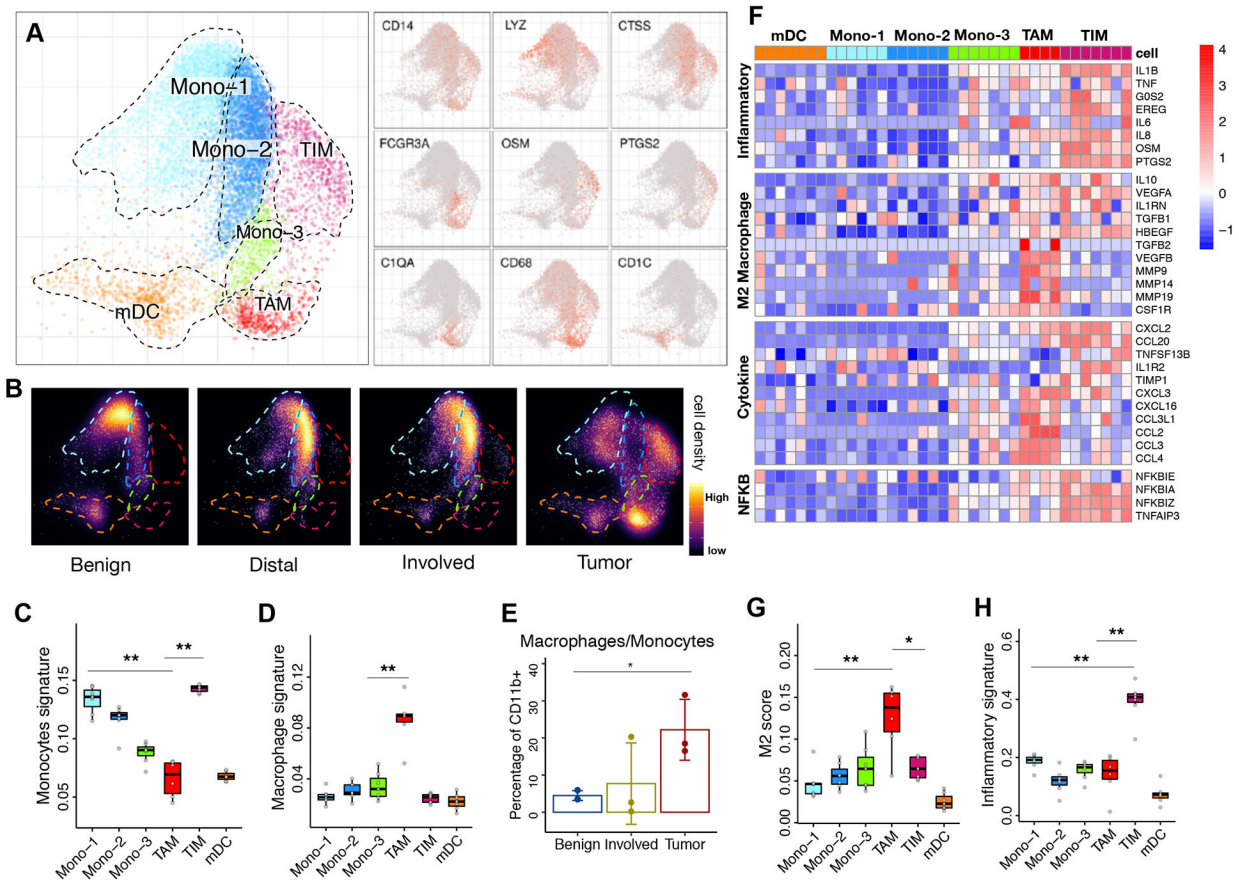

Figure 4. Myeloid populations shift towards inflammatory monocytes and repressive macrophages in the Tumor fraction.

(A) Detailed annotation of the myeloid subpopulations is shown on a myeloid-specific joint embedding (left), together with select gene markers (right).

(B) Changes in the composition of the myeloid compartment between sample fractions is visualized as cell density on the joint embedding.

(C,D) Average expression of monocyte (C) and macrophage (D) signature genes (see STAR Methods, GSE5099) in different myeloid subpopulations shown as boxplot. Statistical significance assessed by Wilcoxon test, reported at 99% reproducibility power (see STAR Methods). Boxplots include centerline(median), 25th to 75th percentiles; and whiskers are highest and lowest values no greater than 1.5x interquartile range.

(E) Barplot showing flow cytometry validation of the monocytes/macrophages abundance from three independent patients. (*p<0.05) by Wilcoxon rank sum test.

(F) Heatmap shows average expression of select genes from different categories (rows) across different cell populations (top color bar, colors matching panel A) for each patient (columns).

(G,H) Average expression of the M2 macrophage signature gene panel (G), and monocyte inflammatory gene panel (H) across different monocyte populations shown as boxplot. Boxplots include centerline(median), 25th to 75th percentiles; and whiskers are highest and lowest values no greater than 1.5x interquartile range.

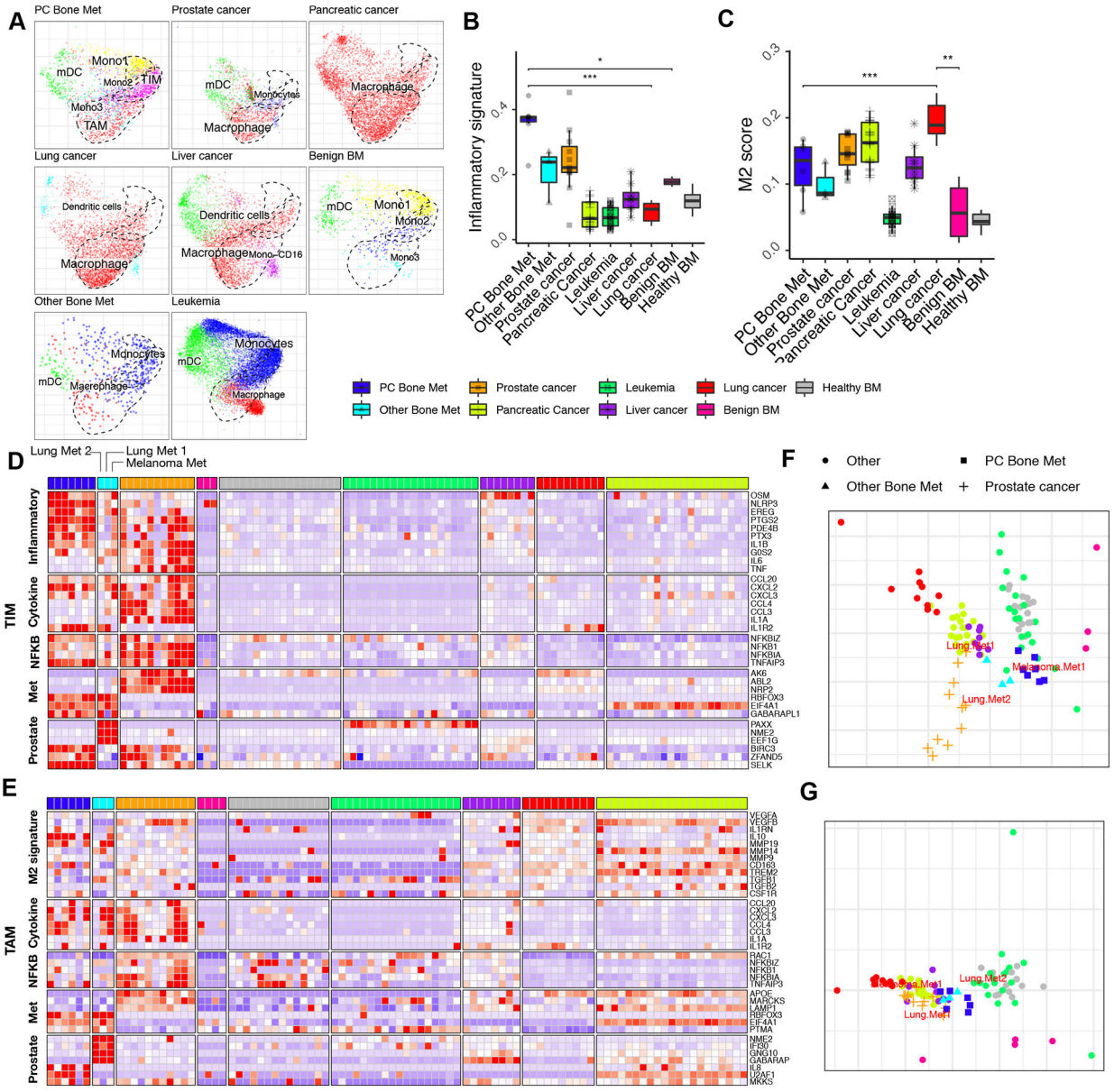

Figure 5. Comparisons of myeloid states with other cancers.

(A) Joint alignment of myeloid cells from different tumor types including other bone metastases (2 lung cancer and 1 melanoma bone metastases. The same contours outline the major myeloid cell populations.

(B,C) Average expression of monocytes inflammatory signatures (B) and M2 macrophage signatures (C) in different cancer types. Boxplots include centerline(median), 25th to 75th percentiles; and whiskers are highest and lowest values no greater than 1.5x interquartile range.

(D,E) Heatmap shows average expression of select genes from different categories (rows) across different cancer types (top color bar, colors matching panel A) for each patient (columns), respectively for TIM (D) and TAM (E).

(F,G) Overall expression similarity of TIM (F) and TAM (G) populations found in different samples is visualized using multidimensional scaling.

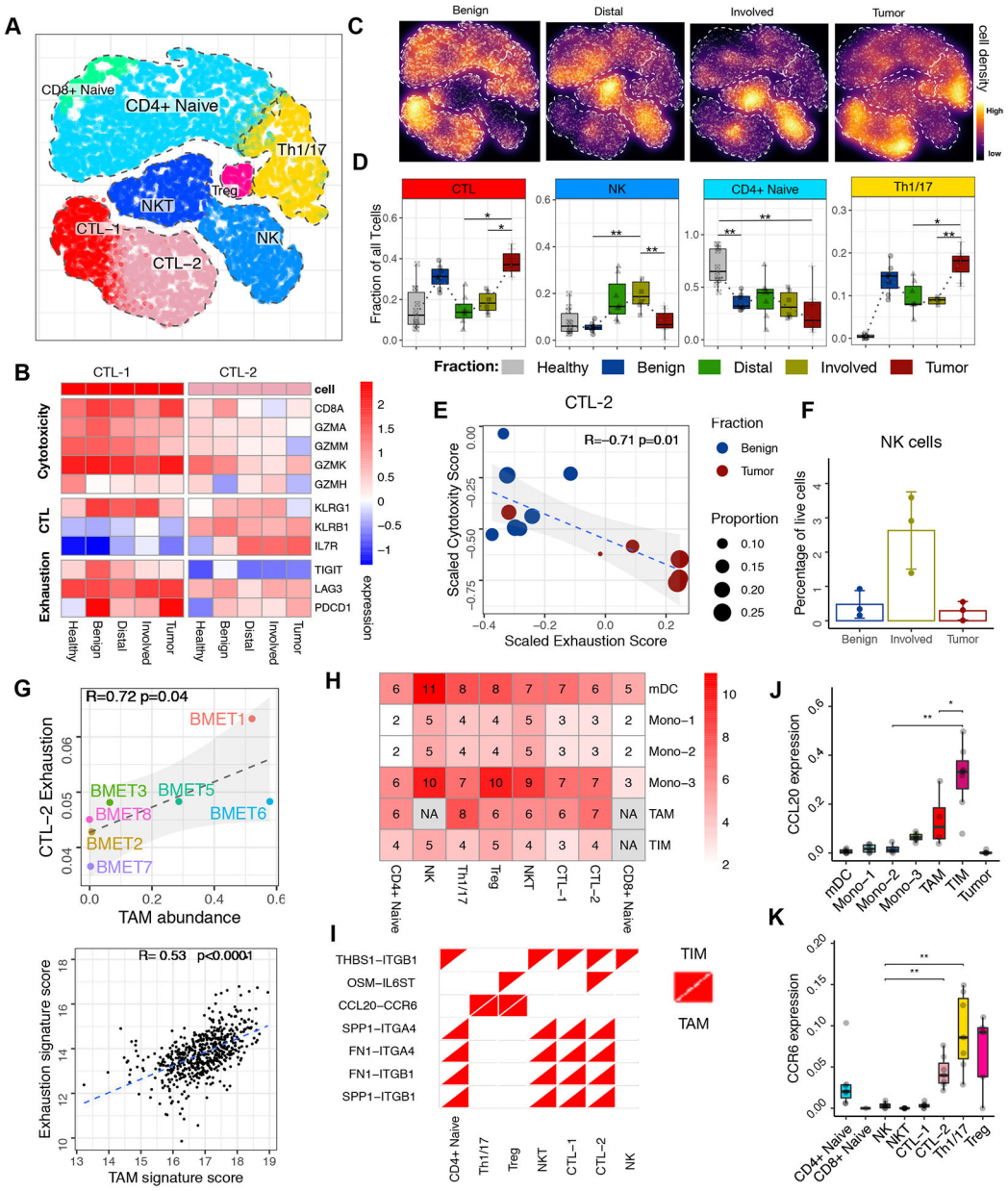

Figure 6. Tumor fraction shows increased abundance of exhausted cytotoxic populations and helper T cells.

(A) Detailed annotation of the T cell subpopulations, shown on a T-cell specific joint embedding.

(B) Expression of key genes from different categories (rows) in CTL-1 and CTL-2 populations across different sample types.

(C) Shifts in the T cell populations visualized as cell density on the joint embedding.

(D) Boxplots of cell frequency changes of different subpopulations between sample fractions. Boxplots include centerline(median), 25th to 75th percentiles; and whiskers are highest and lowest values no greater than 1.5x interquartile range.

(E) Scatter plot showing correlation of cytotoxicity and exhaustion scores for CTL-2 in Benign and Tumor fraction. Statistical significance was assessed using Pearson correlation test.

(F) Barplot showing flow cytometry validation of the NK cell abundance from three independent patients. (*$p<0.05$) by Wilcoxon rank sum test.

(G) The abundance (x axis) of TAM populations is associated with the increased exhaustion of the CTL-2 populations (y axis) (upper). Correlation of TAM signature score and exhaustion signature score is shown as scatter plot for TCGA PRAD bulk RNA-seq data (lower).

(H) The number of known cognate receptor-ligand pairs for which the ligand is expressed in the myeloid subpopulation (rows), and the ligand is expressed in the T cell population (columns).

(I) Receptor-ligand channels connecting TIM and TAM populations to the T cells, based on additional filtering criteria (see STAR Methods).

(J,K) Cluster-average expression of CCL20 (J) and CCR6 (K) is shown for different cell populations. Statistical significance was assessed using Wilcoxon test. Boxplots include centerline(median), 25th to 75th percentiles; and whiskers are highest and lowest values no greater than 1.5x interquartile range.

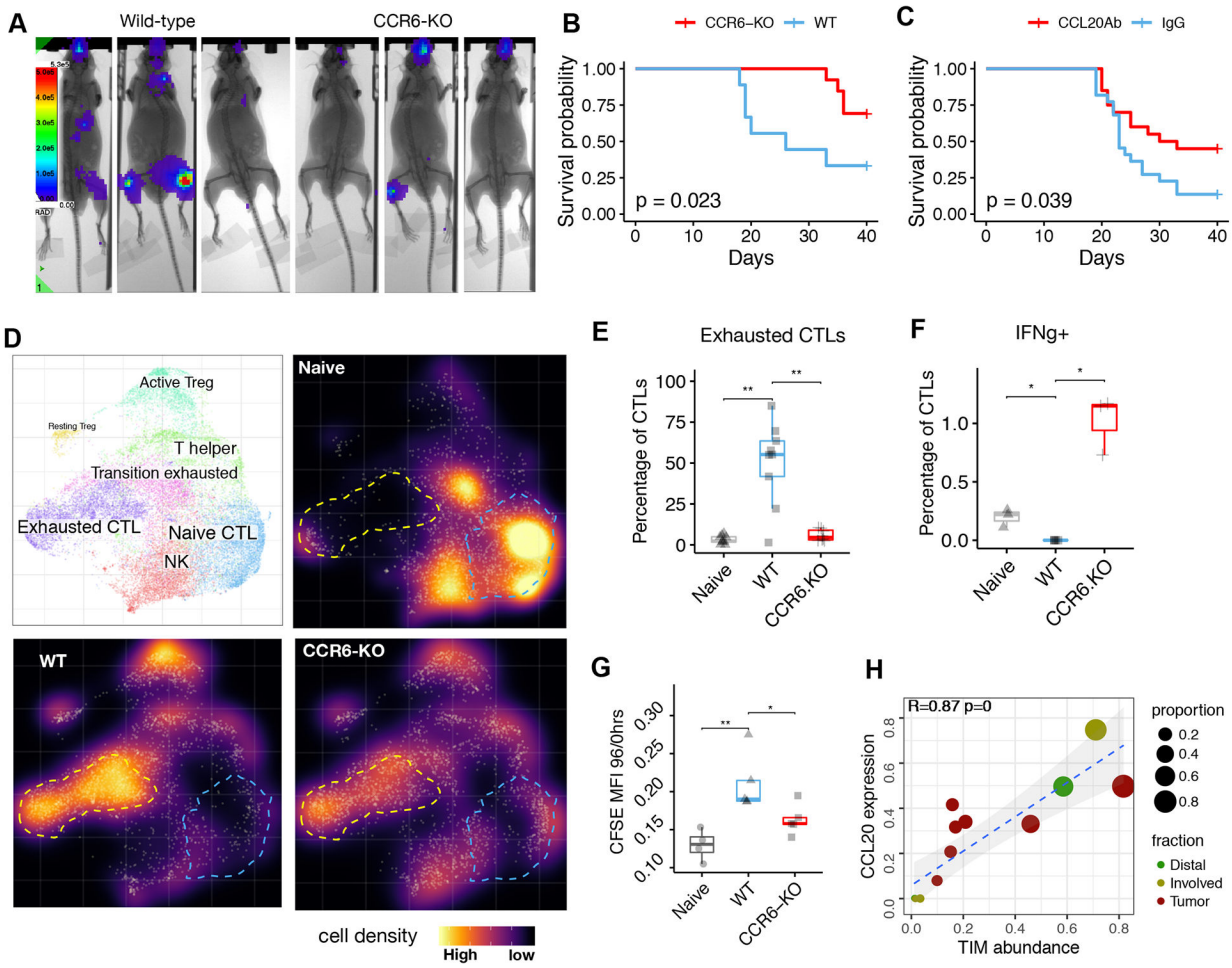

Figure 7. Disruption of the CCL20-CCR6 signaling axis relieves T cell exhaustion and improves survival.

(A) Representative images of bone metastases localization as shown by bioluminescence optical imaging in the mandible or in long bones one week post injection of RM1-BoM3 cells.

(B) CCR6 knockout results in a statistically significant survival benefit in syngeneic mouse model of bone metastases (n=9 WT and n=13 CCR6-KO). Two independent experiments.

(C) Block of CCL20 by antibody results in a statistically significant survival benefit in syngeneic mouse model of bone metastases (n=22 IgG and n=20 CCL20Ab). Two independent experiments.

(D) CD3+ T cells were isolated from the BM and analyzed by single-cell RNA-seq (n=2 mice per group). Changes in the composition of the T cell compartment is visualized as cell density on the joint embedding.

(E) Abundance of Exhausted CTLs populations is shown as a percentage of all CT in mice with BM metastases.

(F) Abundance of IFNg+ CTLs is shown as a percentage of all CTL in mice with BM metastases.

(G) Dilution of CFSE in sorted CTLs was analyzed by flow cytometry after 96 hours of stimulation and compared to baseline levels as an indication of T cell proliferation. (n= 4

naïve, n= 5 WT, n= 5 CCR6-KO). Boxplots in E-G include centerline(median), 25th to 75th percentiles; and whiskers are highest and lowest values no greater than 1.5x interquartile range.

(H) The magnitude of CCL20 expression in the TIM population (y axis) is strongly correlated with the overall abundance of TIM cells, measured as a proportion of all myeloid cells (x axis).

KEY RESOURCES TABLE

REAGENT or RESOURCE	SOURCE	IDENTIFIER
Antibodies		
Lineage (CD3-UCHT1, CD14-HCD14, CD116–3G8, CD19-HIB19, CD20–2H7, CD56-HCD56)-FITC	Biolegend	Cat#348801
CD235-FITC (HIR2)	Biolegend	Cat#306610
CD66b-FITC (G10F5)	Biolegend	Cat#305104
CD38-PeCy7 (HIT2)	Biolegend	Cat#303516
CD24-BV605 (ML5)	Biolegend	Cat#311124
CD34-APCCy7 (581)	Biolegend	Cat#343514
CD11b-BuV737 (M1/70)	BD Biosciences	Cat#564443
CD11c-FITC (Bu15)	Biolegend	Cat#337214
CD14-BV605 (M5E2)	Biolegend	Cat#301834
CD45-BuV395 (HI30)	BD Biosciences	Cat#563792
HLA-DR-APCCy7 (L243)	Biolegend	Cat#307617
CD56-BV711 (NCAM16.2)	BD Biosciences	Cat#563169
CD19-BV711 (HIB19)	Biolegend	Cat#302246
CD3-BV711 (UCHT1)	Biolegend	Cat#300464
CD235-PercpCy5.5 (HIR2)	Biolegend	Cat#306614
CD64-PeDazzle (10.1)	Biolegend	Cat#305032
CD56-PeCy5 (B159)	BD Biosciences	Cat#561904
CD19-BuV737 (SJ25C1)	BD Biosciences	Cat#564304
CD3-BV421 (UCHT1)	Biolegend	Cat#300433
CD4-BV605 (RPA-T4)	Biolegend	Cat#300555
CD8-APCCy7 (RPA-T8)	BD Biosciences	Cat#557760
CD25-APC (M-A251)	Biolegend	Cat#356109
FOXP3-Pe (PCH101)	Thermo Fisher	Cat#12-4776-41
CD45-BV570 (HI30)	Biolegend	Cat#304034
CD3-BuV737 (145–2C11)	BD Biosciences	Cat#612771
CD8-BV570 (53–6.7)	Biolegend	Cat#100740
CD4-AF700 (GK1.5)	Biolegend	Cat#100430
PD-1-Pe (J43)	Thermo Fisher	Cat#12-9985-83
Lag3-PeCy7 (eBioC9B7W)	Thermo Fisher	Cat#25-2231-82
CD4-APCCy7 (GK1.5)	Biolegend	Cat#100526
CD45-BV785 (30-F11)	Biolegend	Cat#103149
IFNg-AF700 (XMG1.2)	Biolegend	Cat#505824
Anti-CCL20 (114908)	R&D	Cat#MAB7601
Rat IgG isotype control (43414)	R&D	Cat#MAB005
Fc block mouse	BD Biosciences	Cat#553142

REAGENT or RESOURCE	SOURCE	IDENTIFIER
Fc block human	BD Biosciences	Cat#564219
Vectors		
Tdtomato/LeGO-T2	Addgene	Cat#27342
Luciferase/pENTR-LUC	Addgene	Cat#17473
Bacterial and virus strains		
Biological samples		
Human bone marrow from prostate bone metastatic cancer patients	Massachusetts General Hospital	
Human prostate/lung/melanoma bone metastases	Massachusetts General Hospital	
Human benign bone marrow from hip replacement surgeries	Massachusetts General Hospital	
Chemicals, peptides, and recombinant proteins		
Critical commercial assays		
Chromium Single Cell 3´v2 Reagent Kit	10X Genomics	N/A
CCL20 ELISA kit	R&D Systems	Cat#DY360
Deposited data		
Data files for scRNA-seq	This paper	GEO: GSE143791
Bulk RNA-seq and clinical data for TCGA cohort	TCGA	https://gdc.cancer.gov/about-data/publications/pancanatlas
Primary prostate cancer scRNA-seq data	Chen et al., 2021	GEO: GSE141445
Pancreatic cancer scRNA-seq data	Peng et al., 2019	GSA: CRA001160
Leukemia scRNA-seq data	Witkowski et al., 2020	GEO: GSE134759
Lung cancer scRNA-seq data	Lambrechts et al., 2018	Arrayexpress: E-MTAB-6149, E-MTAB-6653
Liver cancer scRNA-seq data	Zhang et al., 2019	EGA S00001003449
Healthy Bone marrow scRNA-seq data	Oetjen et al., 2018	GEO: GSE120221, GSE120446
Experimental models: Cell lines		
RM1	Thompson et al., 1989	PMID: 2538247
RM1-BoM1	Power et al., 2009	PMID: 19585491
RM1-BoM3	David Scadden laboratory	N/A
Experimental models: Organisms/strains		
C57BL/6J (males, 8–10 weeks old)	Jackson Laboratory	Cat#00664
B6.129P2-Ccr6tm1Dgen/J	Jackson Laboratory	Cat#005793
Oligonucleotides		
Recombinant DNA		
Software and algorithms		

REAGENT or RESOURCE	SOURCE	IDENTIFIER
Cellranger v2.0	10x Genomics	https://support.10xgenomics.com/single-cell-gene-expression/software/downloads/latest
Conos 1.2.1	Barkas et al., 2019	https://github.com/kharchenkolab/conos
InferCNV	Patel et al., 2014	https://github.com/broadinstitute/inferCNV
ClusterProfiler 4.0 R package	Wu et al., 2021	https://bioconductor.org/packages/release/bioc/html/clusterProfiler.html
Candisc 0.8–5 R package	Comprehensive R Archive Network (CRAN)	https://cran.r-project.org/web/packages/candisc/index.html
Survival 3.2–3 R package	Comprehensive R Archive Network (CRAN)	https://cran.r-project.org/web/packages/survival/index.html
R v3.6.0	https://www.r-project.org/	https://www.r-project.org/
FlowJo software	Treestar	https://www.flowjo.com/
Prism software	GraphPad	https://www.graphpad.com/scientific-%20software/prism/
Other		
Media 199	Thermofisher Scientific	Cat#12350039
DMEM	Thermofisher Scientific	Cat#15–013-CV
RPMI-1640	Thermofisher Scientific	Cat#11875101
Fetal Bovine Serum (FBS)	Life Technologies	Cat#A31605–01
Penicillin-Streptomycin	Life Technologies	Cat#15140–122
STEMxyme1	Worthington	Cat#LS004106
Collagenase type I	Worthington	Cat#LS004214
Collagenase type II	Worthington	Cat#LS004202
Collagenase type III	Worthington	Cat#LS004206
Collagenase type IV	Worthington	Cat#LS004210
Dispase 1	Thermofisher Scientific	Cat#17105041
RNasin Ribonuclease Inhibitor)	Promega	Cat#N2111
RNAase Out Recombinant Ribonuclease Inhibitor	Thermofisher Scientific	Cat#10777019
ACK-lysis buffer	Thermofisher Scientific	Cat#A1049201
Calcein AM	Thermofisher Scientific	Cat#C3099
7-AAD	Thermofisher Scientific	Cat#00-6993-50
DAPI	Thermofisher Scientific	Cat#62248
LIVE/DEAD fixable viability dye	Thermofisher Scientific	Cat#L34961
Cytofix/Cytoperm	BD Biosciences	Cat#554714
Ultrapure BSA	Thermofisher Scientific	Cat#AM2616
BD FACS Aria III	BD Biosciences	
Bioluminescence imaging chamber – SPECTRAL Ami X	Spectral Instruments Imaging	
Dynabeads Mouse T-activator CD3/CD28	Thermofisher Scientific	Cat#11456D
CellTrace CFSE	Thermofisher Scientific	Cat#C34570